Article

Multielectron Redox Chemistry of Iron Porphyrinogens

Julien Bachmann, and Daniel G. Nocera

J. Am. Chem. Soc., **2005**, 127 (13), 4730-4743• DOI: 10.1021/ja043132r • Publication Date (Web): 12 March 2005

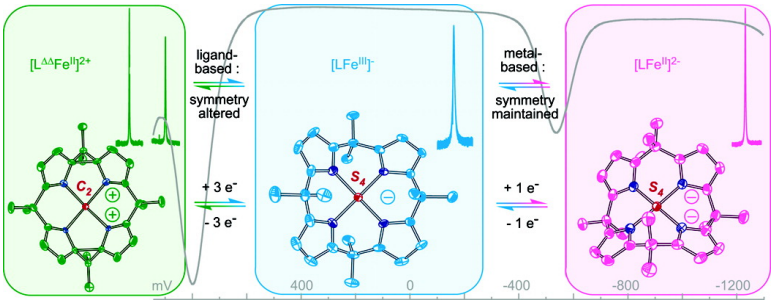

More About This Article

Additional resources and features associated with this article are available within the HTML version:

- Supporting Information
- Links to the 9 articles that cite this article, as of the time of this article download
- Access to high resolution figures
- Links to articles and content related to this article
- Copyright permission to reproduce figures and/or text from this article

View the Full Text HTML

J|A|C|S
ARTICLES
Published on Web 03/12/2005

Multielectron Redox Chemistry of Iron Porphyrinogens

Julien Bachmann and Daniel G. Nocera*

Contribution from the Department of Chemistry, 6-335, Massachusetts Institute of Technology, 77 Massachusetts Avenue, Cambridge Massachusetts 02139-4207

Received November 15, 2004; E-mail: nocera@mit.edu

Abstract: Iron octamethylporphyrinogens were prepared and structurally characterized in three different oxidation states in the absence of axial ligands and with sodium or tetrafluoroborate as the only counterions. Under these conditions, the iron- and ligand-based redox chemistry of iron porphyrinogens can be defined. The iron center is easily oxidized by a single electron ($E_{1/2} = -0.57$ V vs NHE in CH_3CN) when confined within the fully reduced macrocycle. The porphyrinogen ligand also undergoes oxidation but in a single four-electron step ($E_p = +0.77$ V vs NHE in CH_3CN); one of the ligand-based electrons is intercepted for the reduction of Fe(III) to Fe(II) to result in an overall three-electron oxidation process. The oxidation equivalents in the macrocycle are stored in $C^{\alpha}-C^{\alpha}$ bonds of spirocyclopropane rings, formed between adjacent pyrroles. EPR, magnetic and Mössbauer measurements, and DFT computations of the redox states of the iron porphyrinogens reveal that the reduced ligand gives rise to iron in intermediate spin states, whereas the fully oxidized ligand possesses a weaker σ-donor framework, giving rise to high-spin iron. Taken together, the results reported herein establish a metal−macrocycle cooperativity that engenders a multielectron chemistry for iron porphyrinogens that is unavailable to heme cofactors.

Introduction

Iron porphyrin, or heme, is a ubiquitous and versatile protein cofactor. By controlling the heme axial coordination and peptidic environment, proteins may tune cofactor reactivity to selectively perform redox-derived functions as varied as single-electron transfer (cytochromes),[1−13] dioxygen coordination and transport (hemoglobin and myoglobin),[14−17] dioxygen activation and substrate oxidation (cytochrome P-450),[18−23] and peroxide and superoxide removal (peroxidases, catalase).[24−26] Accordingly, the redox properties of iron porphyrins have been investigated intensely as isolated cofactors,[27,28] in the environments of de novo designed[29−37] and natural proteins,[38−51] and in the context of small-molecule substrate activation and catalysis.[52−62] Redox activity of hemes is typically metal centered with the notable

(1) Gray, H. B.; Winkler, J. R. In *Electron Transfer in Chemistry*; Balzani, V., Ed.; Wiley-VCH: Weinheim, Germany, 2001; Vol. 3.1.1, pp 3−23.
(2) Wright, J. L.; Wang, K.; Geren, L.; Saunders: A. J.; Pielak, G. J.; Durham, B.; Millett, F. *Adv. Chem. Ser.* **1998**, *254*, 99−110.
(3) Gray, H. B.; Winkler, J. R. *Annu. Rev. Biochem.* **1996**, *65*, 537−561.
(4) Winkler, J. R.; Gray, H. B. *Chem. Rev.* **1992**, *92*, 369−379.
(5) Tollin, G. In *Electron Transfer in Chemistry*; Balzani, V., Ed.; Wiley-VCH: Weinheim, Germany, 2001; Vol. 4.1.5, pp 202−231.
(6) Wang, K.; Zhen, Y.; Sadoski, R.; Grinnell, S.; Geren, L.; Ferguson-Miller, S.; Durham, B.; Millett, F. *J. Biol. Chem.* **1999**, *274*, 38042−38050.
(7) Nocek, J. M.; Zhou, J. S.; Forest, S. D.; Priyadarshy, S.; Beratan, D. N.; Onuchic, J. N.; Hoffman, B. M. *Chem. Rev.* **1996**, *96*, 2459−2489.
(8) Millett, F. S. *J. Bioenerg. Biomembr.* **1995**, *27*, 261−262.
(9) McLendon, G.; Hake, R. *Chem. Rev.* **1992**, *92*, 481−490.
(10) Scott, R.; Mauk, A. G. *Cytochrome c*: A Multidisciplinary Approach; University Science Books: Sausalito, CA, 1996.
(11) Namslauer, A.; Brzezinski, P. *FEBS Lett.* **2004**, *567*, 103−110.
(12) Namslauer, A.; Braenden, M.; Brzezinski, P. *Biochemistry* **2002**, *41*, 10369−10374.
(13) Qian, J.; Mills, D. A.; Geren, L.; Wang, K.; Hoganson, C. W.; Schmidt, B.; Hiser, C.; Babcock, G. T.; Durham, B.; Millett, F.; Ferguson-Miller, S. *Biochemistry* **2004**, *43*, 5748−5756.
(14) Antonini, E.; Brunori, M. *Hemoglobin and Myoglobin in Their Reactions with Ligands*; North-Holland: Amsterdam, 1971.
(15) Kundu, S.; Trent, J. T.; Hargrove, M. S. *Trends Plant Sci.* **2003**, *8*, 387−393.
(16) Momenteau, M.; Reed, C. A. *Chem. Rev.* **1994**, *94*, 659−698.
(17) Riggs, A. F. *Curr. Opin. Struct. Biol.* **1991**, *1*, 915−921.
(18) *Cytochrome P450*, 2nd ed; Ortiz de Montellano, P. R., Ed.; Plenum Press: New York, 1995.
(19) Makris, T. M.; Davydov, R.; Denisov, I. G.; Hoffman, B. M.; Sligar, S. G. *Drug Metabol. Rev.* **2002**, *34*, 691−708.
(20) Sligar, S. G. *Essays Biochem.* **1999**, *34*, 71−83.
(21) Sono, M.; Roach, M. P.; Coulter, E. D.; Dawson, J. H. *Chem. Rev.* **1996**, *96*, 2841−2887.
(22) Udit, A. K.; Hill, M. G.; Bittner, V. G.; Arnold, F. H.; Gray, H. B. *J. Am. Chem. Soc.* **2004**, *126*, 10218−10219.
(23) Munro, A. W.; Leys, D. G.; McLean, K. J.; Marshall, K. R.; Ost, T. W. B.; Daff, S.; Miles, C. S.; Chapman, S. K.; Lysek, D. A.; Moser, C. C.; Page, C. C.; Dutton, P. L. *Trends Biochem. Sci.* **2002**, *27*, 250−257.
(24) Everse, J.; Everse, K. E.; Grisham, M. B. *Peroxidases in Chemistry and Biology*; CRC Press: Boca Raton, FL, 1991; Vols. I and II.
(25) Erman, J. E.; Hager, L. P.; Sligar, S. G. *Adv. Inorg. Biochem.* **1994**, *10*, 71−118.
(26) Dunford, H. B. *Heme Peroxidases*; John Wiley: Chichester, 1999.
(27) Ozaki, S.-I.; Matsui, T.; Roach, M. P.; Watanabe, Y. *Coord. Chem. Rev.* **2000**, *198*, 39−59.
(28) *The Porphyrin Handbook*; Kadish, K. M., Smith, K. M., Guilard, R., Eds.; Academic Press: New York, 2000; Vol. 9.
(29) Rosenblatt, M. M.; Huffman, D. L.; Wang, X.; Remmer, H. A.; Suslick, K. S. *J. Am. Chem. Soc.* **2002**, *124*, 12394−12395.
(30) Ghirlanda, G.; Osyczka, A.; Liu, W.; Antolovich, M.; Smith, K. M.; Dutton, P. L.; Wand, A. J.; DeGrado, W. F. *J. Am. Chem. Soc.* **2004**, *126*, 8141−8147.
(31) Chen, X.; Discher, B. M.; Pilloud, D. L.; Gibney, B. R.; Moser, C. C.; Dutton, P. L. *J. Phys. Chem. B* **2002**, *106*, 617−624.
(32) Fahnenschmidt, M.; Bittl, R.; Schlodder, E.; Haehnel, W.; Lubitz, W. *Phys. Chem. Chem. Phys.* **2001**, *3*, 4082−4090.
(33) Willner, I.; Heleg-Shabtai, V.; Katz, E.; Rau, H. K.; Haehnel, W. *J. Am. Chem. Soc.* **1999**, *121*, 6455−6468.
(34) Shifman, J. M.; Moser, C. C.; Kalsbeck, W. A.; Bocian, D. F.; Dutton, P. L. *Biochemistry* **1998**, *37*, 16815−16827.
(35) Reedy, C. J.; Kennedy, M. L.; Gibney, B. R. *Chem. Commun.* **2003**, *5*, 570−571.
(36) Moffet, D. A.; Foley, J.; Hecht, M. H. *Biophys. Chem.* **2003**, *105*, 231−9.
(37) Topoglidis, E.; Discher, B. M.; Moser, C. C.; Dutton, P. L.; Durrant, J. R. *ChemBioChem* **2003**, *4*, 1332−1339.
(38) Armstrong, F. A.; Hill, H. A. O.; Walton, N. J. *Acc. Chem. Res.* **1988**, *21*, 407−413.
(39) McMahon, B. H.; Fabian, M.; Tomson, F.; Causgrove, T. P.; Bailey, J. A.; Rein, F. N.; Dyer, R. B.; Palmer, G.; Gennis, R. B.; Woodruff, W. H. *Biochim. Biophys. Acta* **2004**, *1655*, 321−331.

10.1021/ja043132r CCC: $30.25

Chart 1

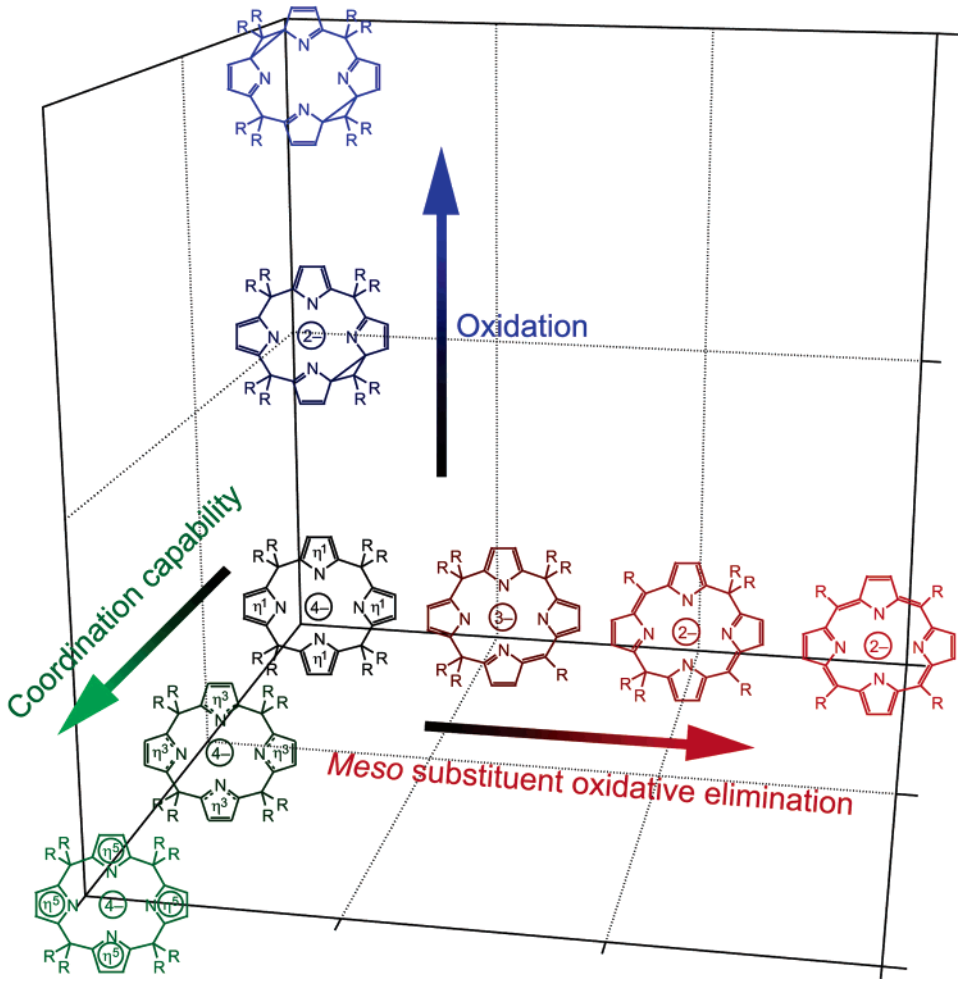

exception of Compound I, which possesses an iron-oxo whose oxidizing power is augmented by a single oxidizing equivalent stored in the porphyrin macrocycle.[63−67] Such a redox activity that is largely confined to the heme metal center reflects a limited cofactor function for the general class of tetrapyrrole coordination compounds.

As illustrated in Chart 1, porphyrins are a chemical subset of a tetrapyrrole family of compounds that have porphyrinogen,[68,69] as an origin. Porphyrins arise from the stepwise oxidation of the porphyrinogen macrocycle coupled to group transfer from the meso positions. Floriani established the first two steps[70−72] of the red branch of Chart 1 and Scott the last

(40) Telford, J. R.; Wittung-Stafshede, P.; Gray, H. B.; Winkler, J. R. *Acc. Chem. Res.* **1998**, *31*, 755−763.
(41) Schultz, B. E.; Chan, S. I. *Proc. Natl. Acad. Sci. U.S.A.* **1998**, *95*, 11643−11648.
(42) McGourty, L. J.; Peterson-Kennedy, S. E.; Ruo, W. Y.; Hoffman, B. M. *Biochemistry* **1987**, *26*, 8302−8312.
(43) Winkler, J. R.; Malmström, B. G.; Gray, H. B. *Biophys. Chem.* **1995**, *54*, 199−209.
(44) Dunn, A. R.; Dmochowski, I. J.; Winkler, J. R.; Gray, H. B. *J. Am. Chem. Soc.* **2003**, *125*, 12450−12456.
(45) Millett, F.; Durham, B. *Photosynth. Res.* **2004**, *82*, 1−16.
(46) Springs, S. L.; Bass, S. E.; Bowman, G.; Nodelman, I.; Schutt, C. E.; McLendon, G. L. *Biochemistry* **2002**, *41*, 4321−4328.
(47) McLendon, G.; Komar-Panicucci, S.; Hatch, S *Adv. Chem. Phys.* **1999**, *107*, 591−600.
(48) Zhou, J. S.; Tran, S. T.; McLendon, G.; Hoffman, B. M. *J. Am. Chem. Soc.* **1997**, *119*, 269−277.
(49) Scott, J. R.; McLean, M.; Sligar, S. G.; Durham, B.; Millett, F. *J. Am. Chem. Soc.* **1994**, *116*, 7356−7362.
(50) Durham, B.; Pan, L. P.; Long, J. E.; Millett, F. *Biochemistry* **1989**, *28*, 8659−8665.
(51) Windsor, M. W.; Holten, D. *Philos. Trans. R. Soc. London, Ser. A* **1980**, *298*, 335−349.
(52) Yeh, C.-Y.; Chang, C. J.; Nocera, D. G. *J. Am. Chem. Soc.* **2001**, *123*, 1513−1514.
(53) Pistorio, B. J.; Chang, C. J.; Nocera, D. G. *J. Am. Chem. Soc.* **2002**, *124*, 7884−7885.
(54) Loh, Z.-H.; Miller, S. E.; Chang, C. J.; Carpenter, S. D.; Nocera, D. G. *J. Phys. Chem. A.* **2002**, *106*, 11700−11708.
(55) Thompson, D. W.; Kretzer, R. M.; Lebeau, E. L.; Scaltrito, D. V.; Ghiladi, R. A.; Lam, K.-C.; Rheingold, A. L.; Karlin, K. D.; Meyer, G. J. *Inorg. Chem.* **2003**, *42*, 5211−5218.
(56) Chng, L. L.; Chang, C. J.; Nocera, D. G. *Org. Lett.* **2003**, *5*, 2421−2424.
(57) Chang, C. J.; Chng, L. L.; Nocera, D. G. *J. Am. Chem. Soc.* **2003**, *125*, 1866−876.
(58) Chang, C. J.; Yeh, C.-Y.; Nocera, D. G. *J. Org. Chem.* **2002**, *67*, 1403−1406.
(59) Collman, J. P.; Wang, Z.; Straumanis, A.; Quelquejeu, M.; Rose, E. *J. Am. Chem. Soc.* **1999**, *121*, 460−461.
(60) Nam, W.; Oh, S.-Y.; Sun, Y. J.; Kim, J.; Kim, W.-K.; Woo, S. K.; Shin, W. *J. Org. Chem.* **2003**, *68*, 7903−7906.
(61) Mansuy, D. *Coord. Chem. Rev.* **1993**, *125*, 129−141.
(62) Collman, J. P.; Boulatov, R.; Sunderland, C. J.; Fu, L. *Chem. Rev.* **2004**, *104*, 561−588.
(63) Watanabe, Y. In *The Porphyrin Handbook*; Kadish, K. M., Smith, K. M., Guilard, R., Eds.; Academic Press: New York, 2000; Vol. 4, pp 97−118.
(64) Schulz, C. E.; Devaney, P. W.; Winkler, H.; Debrunner, P. G.; Doan, N.; Chiang, R.; Rutter, R.; Hager, L. P. *FEBS Lett.* **1979**, *103*, 102−105.
(65) Groves, J. T.; Haushalter, R. C.; Nakamura, M.; Nemo, T. E.; Evans, B. J. *J. Am. Chem. Soc.* **1981**, *103*, 2884−2886.
(66) Penner-Hahn, J. E.; Smith Eble, K.; McMurry, T. J.; Renner, M.; Balch, A. L.; Groves, J. T.; Dawson, J. H.; Hodgson, K. O. *J. Am. Chem. Soc.* **1986**, *108*, 7819−7825.
(67) Nam, W.; Ryu, Y. O.; Song, W. J. *J. Biol. Inorg. Chem.* **2004**, *9*, 654−660.
(68) von Baeyer, J. F. W. A. *Ber.* **1886**, *19*, 2184−2185.
(69) Floriani, C.; Floriani-Moro, R. In *The Porphyrin Handbook*; Kadish, K. M., Smith, K. M., Guilard, R., Eds.; Academic Press: New York, 2000; Vol. 3, pp 385−403.
(70) Bonomo, L.; Solari, E.; Scopelliti, R.; Floriani, C.; Re, N. *J. Am. Chem. Soc.* **2000**, *122*, 5312−5326.

step to deliver porphyrin from porphyrinogen.[73−75] Lying at the fully oxidized terminus of the red branch, the annular ring system of porphyrin displays the aforementioned restricted metal-based redox activity. Two other lines of chemistry evolve from the common porphyrinogen origin as a result of tetrapyrrole-based redox and acid−base transformations. As elaborated by Floriani and Gambarotta using group I, II, IV, and *f*-block ions,[76−83] the green branch results from Lewis acid−base properties of the fully reduced tetrapyrrole macrocycle, which increases its Lewis basicity from η^1 to η^3 and η^5 by tilting pyrroles inward toward the core. The blue branch arises from two-electron oxidation of porphyrinogen to yield the so-called "artificial porphyrins".[84−89] As we have revealed for porphyrinogen containing the element zinc,[90] the tetrapyrrole macrocycle undergoes discrete two-electron oxidations with accompanying formation of one and two spirocyclopropane functionalities.

In contrast to the porphyrins of the red branch of Chart 1, the spectroscopic and redox properties of tetrapyrrole parent compounds on orthogonal branches remain largely unexplored, due principally to the presence of noninnocent ions and ancillary ligands. This problem has been especially pervasive for the blue branch of the artificial porphyrins, which have been isolated as salts of iron halide and polynuclear copper halide counteranions and with axial halide ligands. We now describe the synthesis of the sodium and tetrafluoroborate salts of porphyrinogen macrocycles containing iron. Owing to the absence of redox-active counterions and axial ligands, the oxidation−reduction chemistry of the iron porphyrinogens has been unveiled by electrochemistry, and the various oxidation states have been electronically characterized by spectroscopy and computation. It transpires that iron porphyrinogens possess a one-electron metal-based and four-electron ligand-based chemistry. Metal−organic redox cooperativity engenders a multielectron chemistry of the "artificial hemes" that is unavailable to native heme cofactors.

Experimental Section

Materials. All compounds were handled, reactions were performed, and analytical samples were prepared in inert atmosphere using standard Schlenk, drybox, and vacuum-line techniques. Solvents were purchased from VWR Scientific Products and purified using a Braun solvent purification system or using standard solvent purification techniques.[91] Deuterated solvents were purchased from Cambridge Isotope Laboratories, degassed, dried, and distilled by procedures similar to those used for nonisotopically enriched solvents. Ferrocenium tetrafluoroborate ($FcBF_4$) was purified as previously described.[90] Other reagents were purchased from Aldrich and used as received. Elemental analyses were conducted at H. Kolbe Mikroanalytisches Laboratorium (Mühlheim a. d. Ruhr, Germany). Preparative methods for the d_0 and *meso*-perdeuteriomethyl (d_{24}) versions of each compound were identical; in each case, only one of both is described. Similarly, the only spectroscopic differences observed between both isotopic versions appeared in NMR and IR: reported are the NMR and IR data for the *meso*-perdeuteriomethyl version.

Synthesis of Na(THF)$_2$[LFe]. A milky white suspension of 16.48 g (20.47 mmol) d_{24}-$Na_4(THF)_4L$ in 600 mL of THF was charged with 3.89 g (30.71 mmol, 1.5 equiv) of anhydrous $FeCl_2$ beads (−10 mesh). The resulting mixture was stirred gently overnight with a large magnetic stir bar so that the $FeCl_2$ beads were maintained at the bottom of the flask. Over the course of the first hour of stirring, the mixture turned light green, then beige, brown, and eventually deep red. A gray mixture of NaCl and Fe metal was filtered from the reacted solution; the filtrate was evaporated and dried to yield a solid, which was resuspended in 400 mL of pentane and subsequently stirred for 2 h. The d_{24}-Na(THF)$_2$-[LFe] product was isolated by filtration and dried in vacuo. Yield: 13.02 g (95%) of a deep red powder. The crude product was used for further syntheses. A sample rerystallized from a THF/pentane mixture was used to obtain the following analytical data. ^{1}H NMR (500 MHz, THF-d_8): δ = 13.1 (ax CD_2H), 3.62 (s, THF-α), 1.78 (s, THF-β), −72.2 (br, pyrrole). ^{2}H NMR (76.8 MHz, THF): δ = 13.1 (s, 12H, Me_{ax}), −27.9 (s, 12H, Me_{eq}). UV−vis λ_{max}/nm (ϵ/M^{-1} cm^{-1}) in CH_3CN: 332 (1200), 427 (4800), 526 (3900), ∼570 (sh). IR ν_{max}/cm^{-1} = 3096 m (pyrrole C−H), 2220 s (C−D), 2128 m (C−D), 2060 w (C−D), 1049 s, 917 m, 889 m, 790 w, 750 s. Anal. Calcd for $C_{36}H_{24}D_{24}FeN_4NaO_2$: C 64.36, N 8.34, Fe 8.31; Found: C 64.14, N 8.32, Fe 8.43.

Synthesis of Na$_2$(THF)$_2$[LFe]. Na(THF)$_2$[LFe] (3.00 g, 4.63 mmol), Na metal (0.11 g, 4.63 mmol, 1 equiv) and naphthalene (0.30 g, 2.32 mmol, 0.5 equiv) were mixed in 200 mL of THF. The deep red mixture was refluxed until the foam was white. The cooled deep brown solution was passed through a frit to remove remaining solid Na and the filtrate was brought to dryness by evaporation. The solid $Na_2(THF)_2$[LFe] residue was resuspended in 100 mL of hexane, stirred for 2 h, and eventually filtered and dried in vacuo. Yield: 2.80 g (90%) of brown powder. ^{1}H NMR (500 MHz, THF-d_8): δ = 12.1 (s, ∼0.1H, CD_2H), 3.62 (s, 8H, THF-β), 1.78 (s, 8H, THF-β), −13.3 (br, 8H, pyrrole). ^{2}H NMR (76.8 MHz, THF): δ = 12.1 (s, 12H, Me_{ax}), −46.9 (s, 12H, Me_{eq}). UV−vis λ_{max}/nm (ϵ/M^{-1} cm^{-1}) in CH_3CN: 330 (3300). IR ν_{max}/cm^{-1} = 3086 m (pyrrole C−H), 2218 s (C−D), 2127 m (C−D), 2060 w (C−D), 1268 s, 1049 s, 1036 s, 919 m, 890 w, 791 w, 750 s. Anal. Calcd for $C_{36}H_{48}FeN_4Na_2O_2$: C, 64.48; H, 7.21; N, 8.35; Fe 8.33. Found: C, 64.35; H, 7.26; N, 8.28; Fe 8.32.

Synthesis of [L$^{\Delta\Delta}$Fe](BF$_4$)$_2$. d_{24}-Na(THF)$_2$[LFe] (1.86 g, 2.77 mmol) was dissolved in 50 mL of CH_3CN. Because $[L^{\Delta\Delta}Fe]^{2+}$ was found to be sensitive to ethers, the THF molecules solvating the Na^+ cations had to be removed. The solution was stirred at room temperature for

(71) Benech, J.-M.; Bonomo, L.; Solari, E.; Scopelliti, R.; Floriani, C. *Angew. Chem., Int. Ed.* **1999**, *38*, 1957−1959.
(72) Bonomo, L.; Solari, E.; Martin, G.; Scopelliti, R.; Floriani, C. *Chem. Commun*. **1999**, 2319−2320.
(73) Harmjanz, M.; Gill, H. S.; Scott, M. J. *J. Am. Chem. Soc.* **2000**, *122*, 10476−10477.
(74) Harmjanz, M.; Gill, H. S.; Scott, M. J. *J. Org. Chem.* **2001**, *66*, 5374−5383.
(75) Harmjanz, M.; Božidarević, I.; Scott, M. J. *Org. Lett.* **2001**, *3*, 2281−2284.
(76) Bonomo, L.; Dandin, O.; Solari, E.; Floriani, C.; Scopelliti, R. *Angew. Chem., Int. Ed.* **1999**, *38*, 914−915.
(77) Jacoby, D.; Floriani, C.; Chiesi-Villa, A.; Rizzoli, C. *J. Am. Chem. Soc.* **1993**, *115*, 3595−3602.
(78) Jacoby, D.; Floriani, C.; Chiesi-Villa, A.; Rizzoli, C. *J. Chem. Soc., Chem. Commun.* **1991**, *11*, 790−792.
(79) Bonomo, L.; Solari, E.; Scopelliti, R.; Floriani, C. *Chem. Eur. J.* **2001**, *7*, 1322−1332.
(80) Campazzi, E.; Solari, E.; Scopelliti, R.; Floriani, C. *Chem. Commun*. **1999**, 1617−1618.
(81) Campazzi, E.; Solari, E.; Scopelliti, R.; Floriani, C. *Inorg. Chem*. **1999**, *38*, 6240−6245.
(82) Korobkov, I.; Gambarotta, S.; Yap, G. P. A. *Angew. Chem., Int. Ed.* **2003**, *42*, 814−818.
(83) Korobkov, I.; Gambarotta, S.; Yap, G. P. A. *Angew. Chem., Int. Ed.* **2002**, *41*, 3433−3436.
(84) Floriani, C.; Floriani-Moro, R. In *The Porphyrin Handbook*; Kadish, K. M., Smith, K. M., Guilard, R., Eds.; Academic Press: New York, 2000; Vol. 3, pp 405−420.
(85) Jubb, J.; Floriani, C.; Chiesi-Villa, A.; Rizzoli, C. *J. Am. Chem. Soc.* **1992**, *114*, 6571−6573.
(86) De Angelis, S.; Solari, E.; Floriani, C.; Chiesi-Villa, A.; Rizzoli, C. *J. Am. Chem. Soc*. **1994**, *116*, 5691−5701.
(87) De Angelis, S.; Solari, E.; Floriani, C.; Chies-Villa, A.; Rizzoli, C. *J. Am. Chem. Soc*. **1994**, *116*, 5702−5713.
(88) Piarulli, U.; Solari, E.; Floriani, C.; Chiesi-Villa, A.; Rizzoli, C. *J. Am. Chem. Soc*. **1996**, *118*, 3634−3642.
(89) Crescenzi, R.; Solari, E.; Floriani, C.; Chiesi-Villa, A.; Rizzoli, C. *J. Am. Chem. Soc*. **1999**, *121*, 1695−1706.
(90) Bachmann, J.; Nocera, D. G. *J. Am. Chem. Soc.* **2004**, *126*, 2829−2837.
(91) Armarego, W. L. F.; Perrin, D. D. *Purification of Laboratory Chemicals*, 4th ed.; Butterworth-Heinmann: Oxford, 1996.

10 min, solvent was removed by evaporation, and the remaining solid was dried, redissolved in 50 mL of CH_3CN, and added dropwise to a 50-mL blue CH_3CN solution of $FcBF_4$. The green solution was stirred for 10 min and then again evaporated and dried. The resulting solid was resuspended in 50 mL of CH_2Cl_2 and stirred for 2 h at room temperature, and the beige d_{24}-$[L^{\Delta\Delta}Fe](BF_4)_2/NaBF_4$ solid was separated from the green $Fc/FcBF_4$ supernatant by filtration The desired product was extracted from $NaBF_4$ by boiling the crude mixture in 500 mL of CH_2Cl_2. The resulting suspension was filtered and concentrated to 100 mL. The product was precipitated by dropwise addition of hexanes, and it was isolated by filtration and dried in vacuo. A second harvest of the product, analytically identical to the first, was obtained by performing the extraction procedure an additional time on the original d_{24}-$[L^{\Delta\Delta}Fe](BF_4)_2/NaBF_4$ crude mixture. Combined d_{24}-$[LFe](BF_4)_2$ yield: 1.05 g (56%) of pale beige powder. ^{1}H NMR (500 MHz, CD_3CN): $\delta = 58.7$ (br, 4H, pyrrole), -6.9 (br, 4H, pyrrole). ^{2}H NMR (76.8 MHz, CH_3CN): $\delta = 35.2$ (6H, Me), 9.1 (6H, Me), 4.6 (6H, Me), -2.4 (6H, Me). UV−vis in CH_3CN: far UV ($\lambda_{max} < 230$ nm) band tailing into the visible. IR $\nu_{max}/cm^{-1} = 3115$ m (pyrrole C−H), 2220 w (C−D), 1575 m (C═N), 1564 m (C═N), 1117 s, 1105 s, 1071 s, 1048 s, 1035 s, 1011 s, 855 m. Anal. Calcd for $C_{28}H_8D_{24}FeN_4$: C, 49.59; N, 8.26; Fe, 8.23. Found C, 49.33; N, 8.17; Fe, 8.16.

X-ray Crystal Structure Determinations. X-ray quality crystals were coated with Paratone N oil and mounted on a glass fiber. X-ray diffraction data were collected on a Siemens diffractometer equipped with a CCD detector, using the Mo Kα radiation, selected by a graphite monochromator. The data were integrated to *hkl*-intensity, and the final unit cell was calculated using the SAINT v.4.050 program from Siemens. Solution and refinement were performed with the SHELXTL v.5.03 suite of programs developed by G. M. Sheldrick and Siemens Industrial Automation, 1995. Least-squares refinements were applied to F^2, with hydrogen atoms of organic fragments placed at calculated positions using a standard riding model and refined isotropically.

Red-black crystals of $[(diglyme)_2Na][LFe^{III}]$ were grown from a supersaturated diglyme solution and data were collected at −80 °C. The structure was solved using direct methods; refinement proceeded and converged normally. Red-black crystals of the $\{[(THF)_3Fe^{II}(\mu\text{-}Cl)_3Fe^{II}(THF)_3][(THF)_4Fe^{II}(\mu\text{-}Cl)_2Fe^{II}(THF)_4]_{1/2}\}^{2+}$ salt of $[LFe^{III}]^-$ were grown from a supersaturated THF/toluene solution, and data were collected at −80 °C. The structure was solved using Patterson's method; one of the two toluene solvent molecules contained in the crystal was strongly disordered and could not be properly refined.

Orange crystals containing $[LFe^{II}]^{2-}$ could be grown from pure ethereal solvents but were too oxygen-sensitive to be manipulated, turning instantaneously deep red upon breaking of the sealed ampoule in which they were grown. It was observed that crystals grown from supersaturated THF solution in the presence of pyridine-*N*-oxide were slightly more robust, and a satisfactory dataset for $[(pyO)(THF)Na]_2[LFe^{II}]$ could be collected at −80 °C. The structure was solved using direct methods; refinement proceeded and converged normally.

Despite repeated attempts, $[L^{\Delta\Delta}Fe^{II}]^{2+}$ would not crystallize with BF_4^- as the counterion, but exchange of tetrafluoroborate for cobalticarborane proceeded smoothly in dichloromethane and afforded orange single crystals of $[L^{\Delta\Delta}Fe^{II}(NCCH_3)][(C_2B_9H_{11})_2Co]_2\cdot 2CH_3CN\cdot 2o\text{-}C_6H_4Cl_2$ by slow vapor diffusion of toluene into an *o*-dichlorobenzene/acetonitrile solution. The data were collected at 100 K, and the structure was solved using direct methods. Throughout the refinement, the ^{2}H atoms were treated as natural-abundance H atoms; in the initial stages of refinement, all atoms of the cobalticarborane anions (except for the metal) were treated as borons, then hydrogens were located from the difference map, and finally the carbon atoms were identified by their abnormal anisotropic thermal parameters and abnormal bond distances to hydrogens. In the end, all B−H and C−H distances were fixed to 1.10(±0.10) Å, a value measured for $C_2B_9H_{13}$ by electron diffraction.[92] The crystal was found to be a racemic twin (chiral space group *Abm2*), with absolute structure parameter 0.66(±0.03).

Physical Measurements. ^{1}H NMR spectra were recorded at the MIT Department of Chemistry Instrumentation Facility (DCIF) on a Varian Inova-500 spectrometer, and ^{2}H NMR spectra were recorded on a Varian Inova-500 equipped with an inverse probe. ^{1}H NMR chemical shifts are quoted in ppm relative to tetramethylsilane, and spectra have been internally calibrated to the monoprotio impurity of the deuterated solvent. ^{2}H NMR spectra were referenced to the peak of the monodeuterio impurity of the natural-abundance solvent; the chemical shift was set to be equal to that observed in ^{1}H NMR for the monoprotio impurity of the corresponding deuterated solvent. Spectra were recorded at 20 °C, and a 30-s delay was used between successive pulses to allow for quantitative integration of the solvent peaks in ^{1}H NMR. The quality of the porphyrinogen NMR spectra was sufficiently high that even the $-CD_2H$ isotopic impurity in *meso*-CD_3 (99.9% D) was observable in ^{1}H NMR.

X-band EPR measurements were carried out on frozen solutions at 4.5 K on a Bruker EMX spectrometer; the cavity was maintained at 4.5 K by an Oxford liquid helium cryostat.

Magnetic susceptibilities were determined at 50 Oe on powders contained in gelatin capsules using a Quantum Design MPMSR2 SQUID susceptometer, which was located at MIT Center for Materials Sciences and Engineering; the data were corrected for diamagnetism of the sample holder, and the diamagnetic component of the samples was evaluated from Pascal's constants. The inverse molar paramagnetic susceptibility data, $1/\chi$, were fitted over the entire temperature range according to the following

$$\frac{1}{\chi} = \frac{T-\theta}{C+\chi_{TIP}\cdot(T-\theta)} \qquad (1)$$

where χ_{TIP}, C, and θ are the temperature-independent paramagnetism, the Curie constant, and the Weiss constant, respectively.

Mössbauer absorption data were recorded at 4.2 K on an MS1 spectrometer (WEB Research Co.) equipped with a ^{57}Co source and a Janus cryostat, and referenced to elemental iron.

UV−visible absorption spectra were recorded on a Spectral Instruments 440 spectrophotometer. Molar absorptivity coefficients were determined on solutions of submillimolar concentrations of iron porphyrinogens. IR absorption spectra on solids dispersed in Nujol mulls were recorded on a Perkin-Elmer 2000 FT-IR spectrophotometer.

Electrochemistry was performed with a standard three-electrode configuration using a CV-50W potentiostat (Bioanalytical Systems). The working electrode was Pt, the auxiliary electrode was a Pt wire, and the reference was an $Ag/AgNO_3$ electrode, which was externally referenced to the Fc^+/Fc couple ($E°(Fc^+/Fc) = 0.65$ V (in CH_3CN) and 0.69 V (in THF) vs NHE).[93] All potentials reported are vs NHE. The most well-behaved electrochemistry was observed for the tetrabutylammonium (Bu_4N^+) salts of the $[LFe^{III}]^-$ and $[LFe^{II}]^{2-}$ anions, which were prepared by adding a stoichiometric amount of Bu_4NCl to a THF solution of the Na^+ salts of the respective complexes. The white NaCl precipitate was separated from the reaction mixture by filtration, and the desired product was obtained by evaporating THF from the filtrate under vacuum. The remaining solid was triturated in hexanes and isolated by filtration. Cyclic voltammetry (CV), differential pulse polarography (DPP), and chronocoulometry experiments were conducted on a CH_3CN solution containing 1 mM $(Bu_4N)[LFe^{III}]$ and 0.04 M Bu_4NBPh_4. CV scans were initiated from the solution's resting potential at 100 mV/s. The scan rate dependence of CV waves were recorded over the potential range of 50−600 mV/s. DPP was performed by polarizing the working electrode at an initial, negative potential for 2 s and then scanning the potential axis in the positive direction. In the chronocoulometry experiment, the working electrode was poised at 311 mV for 2 s, after which it was jumped to either −899 or 911 mV. The

(92) Mackie, I. D.; Robertson, H. E.; Rankin, D. W. H.; Fox, M. A.; Malget, J. M. *Inorg. Chem.* **2004**, *43*, 5387−5392.
(93) Connelly, N. G.; Geiger, W. E. *Chem. Rev.* **1996**, *96*, 877−910.

Scheme 1

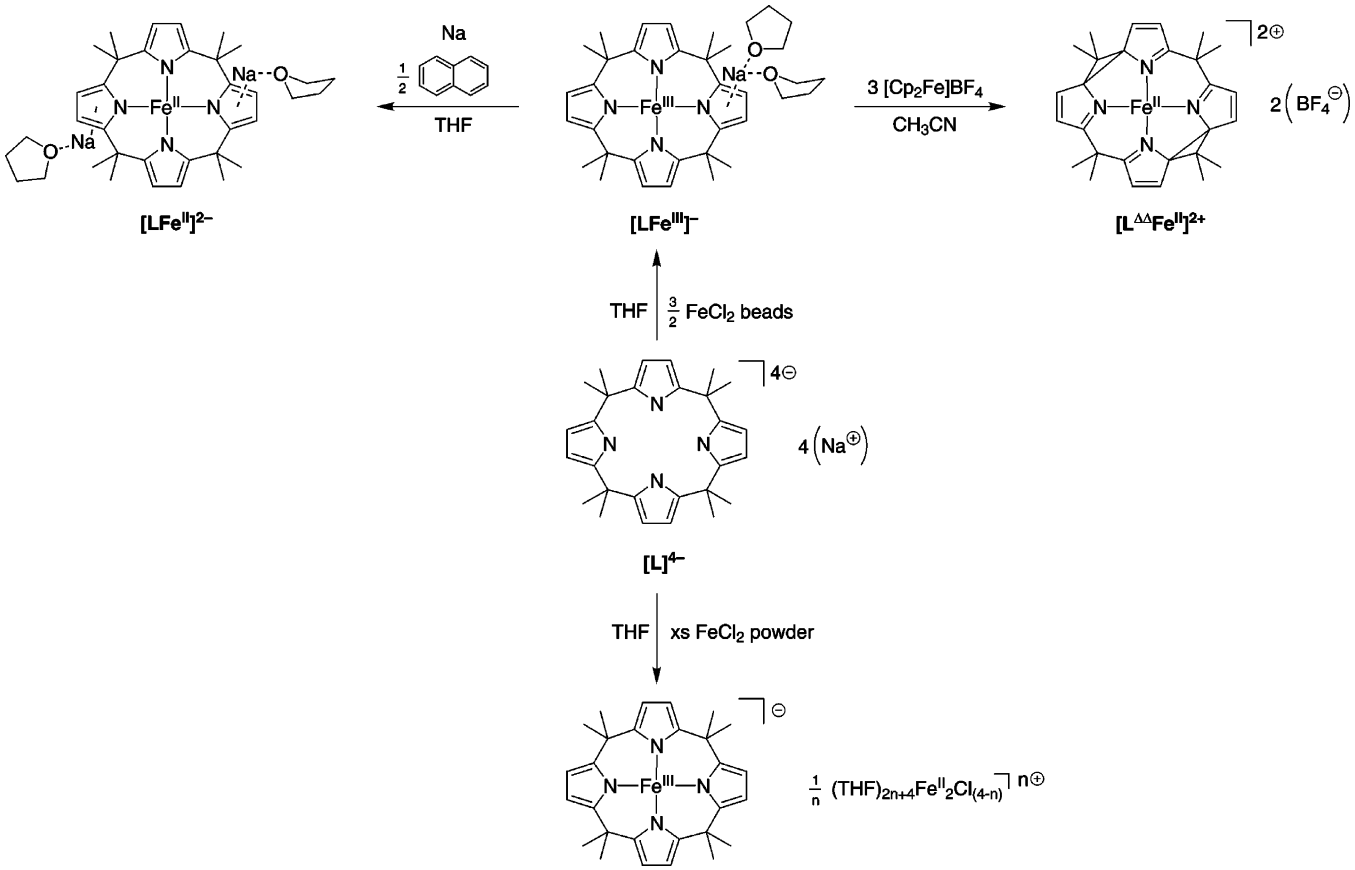

total charge that was passed through the electrode was measured for 250 ms. The resulting curves were analyzed and fitted in their linear regime by the CV-50W software using a least-squares procedure.

Computational Methods. Density functional theory calculations (DFT) were performed using the Amsterdam Density Functional (ADF2002.02) program[94,95] on a home-built Linux cluster comprising 60 Intel processors organized in groups of 12 running in parallel. The generalized gradient approximation was used as implemented in ADF by the Becke-88 functional for exchange,[96] and the Perdew−Wang-91 functional for correlation.[97] A basis set of triple-ζ Slater-type functions augmented by a polarization set (TZP) was used for Fe and N atoms and double-ζ with polarization (DZP) for other atoms, with frozen core approximation; spin restriction was lifted for all $S \neq 0$ cases. Energies reported are gas-phase internal energies at 0 K, without zero-point vibrational energy, of the entity in the experimental solid-state structure. Orbitals were visualized using the Molekel v.4.2 Linux-mesa software.[98,99]

Results and Discussion

Synthesis. Scheme 1 outlines the syntheses of the iron porphyrinogens that are the focus of this study. Control of the availability of solubilized $FeCl_2$ is essential to obtaining the parent complex $[LFe^{III}]^-$ in the absence of iron-based anions. We find that heterogeneous introduction of Fe^{2+} ion into solution with gentle stirring is critical to the success of this chemistry, with $FeCl_2$ beads (−10 mesh) serving as the Fe^{2+} source. Reaction mixtures containing the free base porphyrinogen macrocycle, designated $[L]^{4-}$, and the $FeCl_2$ beads turn the very deep red color that is characteristic of the presence of the $[LFe^{III}]^-$ complex after ∼1 h. The direct insertion product, $[LFe^{II}]^{2-}$, was not observed during the course of the reaction because it is oxidized in situ to $[LFe^{III}]^-$ by $FeCl_2$ (consistent with the observed formation of black Fe metal powder during the reaction). Under the heterogeneous synthesis conditions, $[LFe^{III}]^-$ is isolated as the sodium salt. The absence of iron-containing countercations was confirmed by elemental analysis, single-crystal X-ray diffraction analysis, and by Mössbauer spectroscopy.

Complications arise if the iron center is installed into the macrocycle according to established procedures.[86−88] Tetrahydrofuran suspensions of Na_4L charged with $FeCl_2$ *powder* turn deep red within minutes, and $[LFe^{III}]^-$ is isolable as a salt of Fe^{II}_2-based countercations, $[(THF)_4Fe(\mu\text{-}Cl)_2Fe(THF)_4]_{1/2}$-$[(THF)_3Fe(\mu\text{-}Cl)_3Fe(THF)_3][LFe]_2$ (see Scheme 1). The very low solubility of Na_4L with respect to $FeCl_2$ in THF presumably yields to a preponderance of Fe^{2+} in solution during metalation, thereby favoring formation of the bimetallic cations followed by their subsequent metathesis with the Na^+ ion. This wayward chemistry is observed despite a stoichiometric $Na_4L/FeCl_2$ ratio and the employment of methods for the slow addition of $FeCl_2$ to solution. Indeed, the only way we found to prevent the buildup of Fe^{2+} in solution was the utilization of the heterogeneous reaction conditions described in the foregoing paragraph. Given the abundance of Fe^{n+} centers in $[(THF)_4Fe$-$(\mu\text{-}Cl)_2Fe(THF)_4]_{1/2}[(THF)_3Fe(\mu\text{-}Cl)_3Fe(THF)_3][LFe]_2$, different combinations of formal charges for the constituent Fe^{n+} ions

(94) te Velde, G.; Bickelhaupt, F. M.; van Gisbergen, S. J. A.; Fonseca Guerra, C.; Baerends, E. J.; Snijders, J. G.; Ziegler, T. *J. Comput. Chem.* **2001**, *22*, 931−967.
(95) Fonseca Guerra, C.; Snijders, J. G.; te Velde, G.; Baerends, E. J. *Theor. Chem. Acc.* **1998**, *99*, 391−403.
(96) Becke, A. D. *Phys. Rev. A* **1988**, *38*, 3098−3100.
(97) Perdew, J. P.; Chevary, J. A.; Vosko, S. H.; Jackson, K. A.; Pederson, M. R.; Singh, D. J.; Fiolhais, C. *Phys. Rev. B* **1992**, *46*, 6671−6687.
(98) Flükiger, P.; Lüthi, H. P.; Portmann, S.; Weber, J. *Molekel*, v.4.2/3; Swiss Center for Scientific Computing: Manno, Switzerland, 2000−2002.
(99) Portmann, S.; Lüthi, H. P. *Chimia* **2000**, *54*, 766−769.

may satisfy the overall charge balance. The formal oxidation states in this compound are assigned by inspection of its X-ray crystal structure, which is supplied as Supporting Information (Figure S1). The metrics of the $[(THF)_3Fe(\mu\text{-}Cl)_3Fe(THF)_3]^{n+}$ complex cation (Table S1, Supporting Information) are identical to those of the cation in the previously reported salt, $[(THF)_3Fe^{II}(\mu\text{-}Cl)_3Fe^{II}(THF)_3][(THF)Sn^{IV}Cl_5]$.[100] Additionally, the metrics of the porphyrinogen anion are identical to those of the crystal structure of $[Na(solv)_2][LFe^{III}]$ (Table S1), thus setting a formal charge of +2 for the iron centers in the $[(THF)_4Fe(\mu\text{-}Cl)_2Fe(THF)_4]^{2+}$ complex cation.

The $[LFe^{III}]^-$ complex served as the parent complex for the other series members. The one-electron reduced congener $[LFe^{II}]^{2-}$ is afforded in quantitative yield by the reduction of $[LFe^{III}]^-$ with a stoichiometric or excess amount of sodium naphthalenide. This material is very air sensitive, sometimes smoldering upon exposure to air. The Na^+ ions may be exchanged with tetrabutylammonium using Bu_4NCl in THF.

Alternatively, $[LFe^{III}]^-$ may be oxidized by ferrocenium tetrafluoroborate ($FcBF_4$) in CH_3CN. $[L^{\Delta\Delta}Fe^{II}](BF_4)_2$ is obtained as the only isolable iron product, regardless of the $Na[LFe^{III}]/FcBF_4$ ratio. An insoluble brown byproduct was not characterized. Care was taken in the choice of the starting material. Ethers appear to favor radical processes and exacerbate the subsequent decomposition of the oxidized product. Consequently, $[Na(solv)_2][LFe^{III}]$ where solv = THF was avoided. Three equivalents of $FcBF_4$ are consumed in the reaction as ascertained by recovery of the Fc reduction product; for preparative convenience, three equivalents of $FcBF_4$ were therefore employed for the oxidation. The macrocycle undergoes a selective four-electron oxidation from $[L]^{4-}$ to $L^{\Delta\Delta}$ (with subsequent reduction of Fe^{III} to Fe^{II}), and under no conditions is a product obtained with the macrocycle oxidized by two electrons (i.e., $[L^{\Delta}]^{2-}$). Consistent with this result, $[L^{\Delta\Delta}Fe^{II}]^{2+}$ and $[LFe^{III}]^-$ do not undergo a comproportionation reaction. $[L^{\Delta\Delta}Fe^{II}](BF_4)_2$ does not thermally decompose in the solid state, in acetonitrile solution, or as a dichloromethane suspension at room temperature. However, salt metathesis attempts in dichloromethane with sodium tetraphenylborate caused decomposition on the time scale of dissolution of the reactants (as witnessed by a color change from yellow to brown and the complete loss of the NMR signals of $[L^{\Delta\Delta}Fe^{II}]^{2+}$). For the purpose of growing large single crystals suitable for X-ray analysis, sodium cobalticarborane, $Na[(C_2B_9H_{11})_2Co]$, was employed for salt metathesis, which proceeded very cleanly in CH_2Cl_2.

Published work shows that the iron center of $[L^{\Delta\Delta}Fe^{II}]^{2+}$ may be oxidized when chloride is available to coordinate axially, yielding $[L^{\Delta\Delta}Fe^{III}Cl]^{2+}$.[86] The oxidation, however, does not proceed easily in the absence of noncoordinating, "innocent" counteranions. For instance, treatment of $[L^{\Delta\Delta}Fe^{II}]^{2+}$ with the strongly oxidizing thianthrenium radical cation[101] was accompanied by the disappearance of the deep purple color of the radical cation, but most of the $[L^{\Delta\Delta}Fe^{II}]^{2+}$ starting material was recovered.

Structural Chemistry. The structures of the iron porphyrinogen frameworks of $[LFe^{II}]^{2-}$, $[LFe^{III}]^-$, and $[L^{\Delta\Delta}Fe^{II}]^{2+}$ are shown in Figure 1. Crystallographic data and selected geometrical measurements for the three structures are given in Tables 1 and 2, respectively. The structure of $[LFe^{II}]^{2-}$ and $[LFe^{III}]^-$ are similar to each other and to that previously reported for the dilithium salt of iron(II) octaethylporphyrinogen. As is most easily seen from the edge-on perspective, the central iron ion lies in a nearly perfect planar tetracoordinate environment defined by the four pyrrole nitrogens (4-N), and no significant intermolecular contacts are observed. Owing to the sp^3 hybridization of the meso carbons, the pyrroles cant about the N−Fe−N two-fold axes. The two structures are distinguished by the Fe−N bond lengths of the macrocycle core. As expected, the Fe−N bond is significantly longer for the iron center possessing the greater valence electron count (d_{avg}(Fe−N) = 1.933 Å in $[LFe^{II}]^{2-}$ vs d_{avg}(Fe−N) = 1.899 Å in $[LFe^{III}]^-$). The only other significant differences in the structures result directly from the countercations (which are not shown in Figure 1 but included in Figures S3−S6). The Na^+ countercation of $[LFe^{III}]^-$ assumes a pseudo-octahedral coordination defined by the oxygens of two *fac*-diglyme solvent molecules. The Na^+ countercations of $[LFe^{II}]^{2-}$ are coordinated by diametrically opposite pyrroles in a η^4 fashion (d_{avg}(Na···N) = 3.07 Å) is significantly longer than d_{avg}(Na−C) = 2.80 Å) residing on opposite faces of the macrocycle. The remaining coordination sites of the Na^+ ions are occupied by three monodentate oxygen ligands, one from THF and two from symmetry-related bridging pyridine-*N*-oxides (which create a coordination polymer in the lattice). The latter coordinate the alkali cations and attenuate the very high oxygen sensitivity of the crystals (which in the absence of pyridine-*N*-oxide quickly turn from golden orange to deep red upon manipulation).

The X-ray crystal structures of $[LFe^{II}]^{2-}$ and $[LFe^{III}]^-$ indicate no direct bonding interaction between the α-carbons of adjacent pyrroles ($d_{avg}(C^{\alpha}-C^{\alpha})$ = 2.47 Å in $[LFe^{III}]^-$ and $d_{avg}(C^{\alpha}-C^{\alpha})$ = 2.50 Å in $[LFe^{II}]^{2-}$). This observation is consistent with no oxidation of the macrocycle. Conversely, two pairs of adjacent C^{α} atoms of the $[L^{\Delta\Delta}Fe^{II}]^{2+}$ macrocycle are within single bond distance of each other ($d(C^{\alpha}-C^{\alpha})$ = 1.607(11) Å and 1.553(13) Å). The cyclopropanes are nearly equilateral triangles with $C^{\alpha}-C^{meso}-C^{\alpha}$ angles of 63.3(6)° and 62.3(7)°. These metrics of the cyclopropane rings are similar to those observed in previously described dicyclopropane octaethylporphyrinogens of iron, manganese, and cobalt.[84,86−88]

The presence of the spirocyclopropane rings distorts the macrocycle and the constituent pyrroles. The presence of alternating formal single and double bonds in the pyrroles is plainly evident: N=C double bonds (d_{avg}(N(1)−C(4), (N(2)−C(8)) = 1.31 Å) are significantly shorter than their neighboring N−C single bonds (d_{avg}(N(1)−C(1), N(2)−C(11)) = 1.45 Å). The $C^{\alpha}-C^{\alpha}$ straps constrain the macrocycle along one axis, causing the 4-N core to deform from a square to a rectangle (∠(N(1)−Fe−N(2)) = 87.3° and ∠(N(1)−Fe−N(1A)) = 79.5°). The ruffled conformation of the $[L]^{4-}$ macrocycle is supplanted by a bowl conformation in $[L^{\Delta\Delta}]$, as observed in calixarenes[102] and calixpyrroles,[103−107] in which all four pyrrole planes are

(100) Janas, Z.; Sobota, P.; Lis, T. J. *Chem. Soc. Dalton Trans.* **1991**, 2429−2434.
(101) Lee, W. K.; Lio, B.; Park, C. W.; Shine, H. J.; Guzman-Jimenez, I. Y.; Whitmire, K. H. *J. Org. Chem.* **1999**, *64*, 9206−9210.
(102) Gutsche, C. D.; Muthukrishnan, R. *J. Org. Chem.* **1978**, *43*, 4905−4906.
(103) Gale, P. A.; Sessler, J. L.; Lynch, V.; Sansom, P. I. *Tetrahedron* Lett. **1996**, *37*, 7881−7884.
(104) Anzenbacher, P., Jr.; Jursíková, K.; Lynch, V. M.; Gale, P. A.; Sessler, J. L. *J. Am. Chem. Soc.* **1999**, *121*, 11020−11021.
(105) Sessler, J. L.; Anzenbacher, P., Jr.; Miyaji, H.; Jursiková, K.; Bleasdale, E. R.; Gale, P. A. *Ind. Eng. Chem. Res.* **2000**, *39*, 3471−3478.
(106) Nielsen, K. A.; Jeppesen, J. O.; Levillain, E.; Becher, J. *Angew.* Chem., Int. Ed. **2003**, *42*, 187−191.

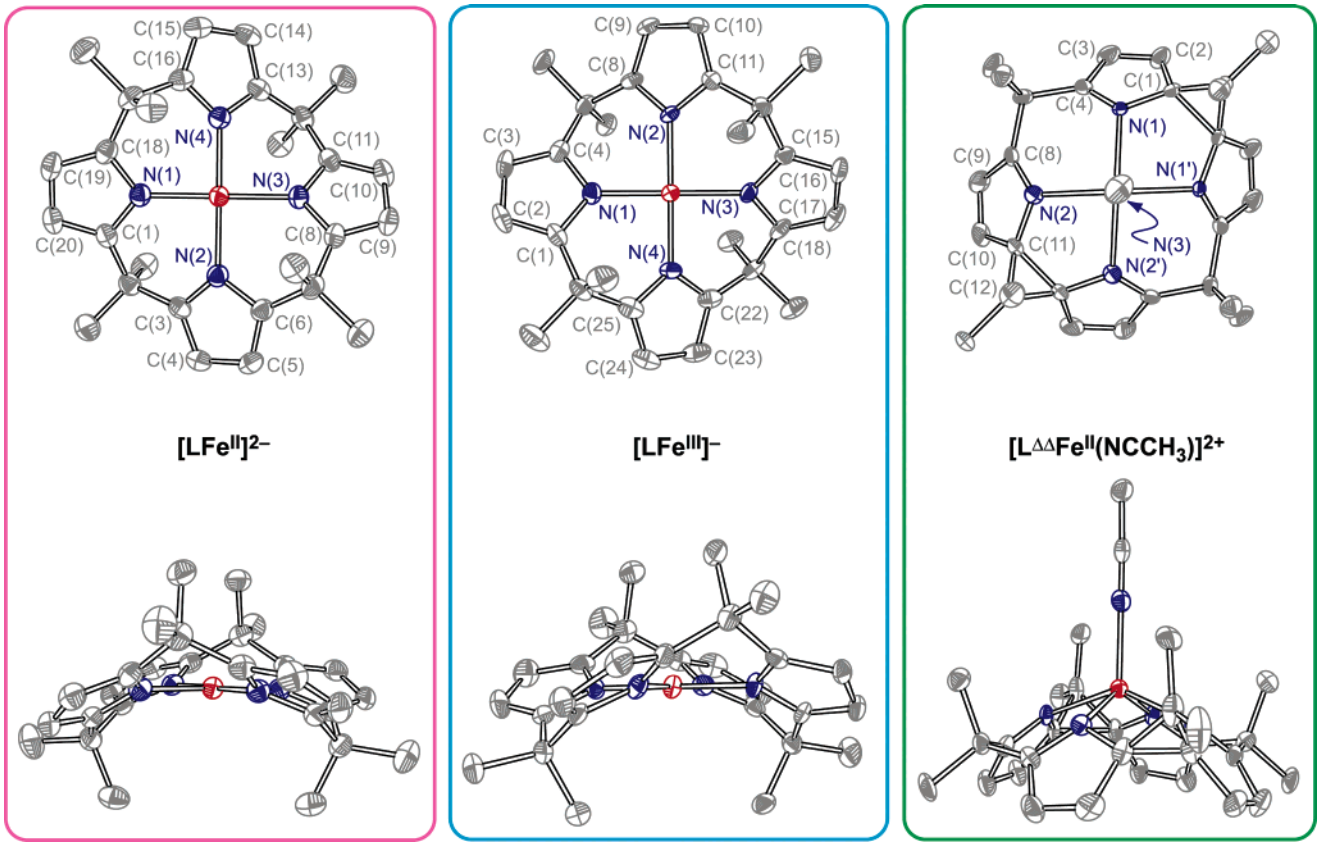

Figure 1. Comparative views of the solid-state structures of the iron porphyrinogen frameworks in $[(THF)Na(Opy)]_2[LFe^{II}]$, $[Na(diglyme)_2][LFe^{III}]$, and $[d_{24}\text{-}L^{\Delta\Delta}Fe^{II}(NCCH_3)][(C_2B_9H_{11})_2Co]_2$: (top) top view, perpendicular to the 4-N plane; (bottom) side view, parallel to the 4-N plane. Thermal ellipsoids are drawn at the 50% probability level, and H atoms and counterions and solvent molecules are omitted for clarity. The color coding of pink for data associated with $[LFe^{II}]^{2-}$, blue for data associated with $[LFe^{III}]^{-}$, and green for data associated with $[L^{\Delta\Delta}Fe^{II}(NCCH_3)]^{2+}$ is maintained throughout this manuscript.

tilted upward relative to the N_4 plane. The conformational change from ruffle to bowl is accompanied by the movement of the Fe^{II} center from the 4-N plane by 0.72 Å. The displaced Fe^{II} center coordinates an axial CH_3CN solvent molecule to engender a distorted square pyramidal coordination geometry. The four-electron oxidized macrocycle is a much weaker donor than the parent $[L]^{4-}$ porphyrinogen, as evidenced by long Fe−N(pyrrole) bonds; the d_{avg}(Fe−N(pyrrole)) = 2.12 Å is 0.18 Å longer than the Fe−N(pyrrole) bond lengths of $[LFe^{II}]^{2-}$ and is longer than the Fe−N bond to the axial CH_3CN (d(Fe−N(3)) = 2.065 Å). All five Fe−N distances in this free $[L^{\Delta\Delta}Fe^{II}(NCCH_3)]^{2+}$ entity, however, are significantly shorter than the corresponding ones in the previously reported polynuclear compound $[L^{\Delta\Delta}Fe^{II}(Cl)(Cu_4Cl_5)]$, indicating that the interacting $Cu_4Cl_5^-$ influences the structural properties of the iron porphyrinogen moiety.[89] Our results establish the stable existence of and intrinsic metrics for $[L^{\Delta\Delta}Fe^{II}L]^{2+}$ in the absence of an anionic axial ligand and an interacting counterion.

Paramagnetic ^{1}H and ^{2}H NMR. The porphyrinogen framework was synthesized with deuterated meso methyls, allowing the solution structures of the series members to be probed by ^{1}H and ^{2}H NMR. As displayed in Figure 2, exceptionally high-quality NMR spectra are obtained despite the presence of the paramagnetic iron centers. Owing to the meso d_{24} substitution, the hydrogens on the methyl groups and pyrroles can be investigated in separate experiments and therefore are easily distinguished from each other.

The single resonance for the eight pyrrole hydrogens observed in the ^{1}H NMR spectra of $[LFe^{II}]^{2-}$ and $[LFe^{III}]^{-}$ in solution (Figure 2, top and middle trace, respectively) is consistent with the four-fold symmetry of the porphyrinogen in the solid state. The ^{2}H NMR spectrum of these compounds is also consistent with this four-fold symmetry but two signals of equal intensity are observed for the meso methyls. The two distinct signals reflect a symmetry lower than D_{4h}, arising from either (i) coordination of the Na^+ ions to the one side of the macrocycle or (ii) retention of the D_{2d} conformation of the solid-state structure for the molecules in solution. The invariance of the ^{2}H NMR spectrum to solvent (THF, diglyme, or acetonitrile), to encryption of Na^+ by 18-crown-6 ether, and to replacement of Na^+ by NBu_4^+ rules out possibility (i); thus, the chair conformation of the tetrapyrrole observed in the solid state is retained in solution. The two peaks are ascribed to the axial and equatorial meso methyl positions (axial being defined as close to perpendicular to the 4-N plane, and equatorial being defined as close to parallel to that plane). This interpretation is further corroborated by the relative magnitudes of the paramagnetic shifts for the axial and equatorial methyl resonances. The paramagnetic shift, $\Delta\nu_{pc}/\nu$, of a nucleus at a position (r, θ, ϕ) relative to the paramagnetic iron center is given by

$$\frac{\Delta\nu_{pc}}{\nu} = \frac{\mu_0}{4\pi}\cdot\frac{\beta^2 S(S+1)}{9kT}\cdot\frac{3\cos^2\theta - 1}{r^3}\cdot(g_{par}{}^2 - g_{perp}{}^2) \quad (2)$$

as long as the system has axial symmetry, the electron spin resides exclusively at iron, and the dipole coupling is purely

(107) Yoon, D.-W.; Hwang, H.; Lee, C.-H. *Angew.* Chem., Int. Ed. **2002**, *41*, 1757−1759.

Table 1. Summary of Crystallographic Data for Iron Porphyrinogens

	[(THF)Na(Opy)]$_2$[LFe^{II}]	[Na(diglyme)$_2$][LFe^{III}]	[L$^{\Delta\Delta}$Fe^{II}(NCCH$_3$)][(C$_2$B$_9$H$_{11}$)$_2$Co]$_2$·2CH$_3$CN·2*o*-C$_6$H$_4$Cl$_2$
empirical formula	$C_{50}H_{58}FeN_6Na_2O_4$	$C_{40}H_{60}FeN_4NaO_6$	$C_{54}H_{85}B_{36}Cl_4Co_2FeN_7$
formula weight	908.85	771.76	1536.96
T (K)	183(2)	183(2)	100(2)
λ (Å)	0.71073	0.71073	0.71073
crystal system	monoclinic	orthorhombic	orthorhombic
space group	$P2_1/c$	*Pbca*	*Abm*2
a (Å)	20.4824(13)	15.5367(12)	23.443(2)
b (Å)	11.6675(7)	21.1012(16)	25.146(3)
c (Å)	19.2151(12)	25.2473(19)	13.2883(13)
α (deg)	90	90	90
β (deg)	102.4720(10)	90	90
γ (deg)	90	90	90
V (Å^3)	4483.6(5)	8277.2(11)	7833.6(14)
Z	4	8	4
crystal size (mm^3)	0.27 × 0.27 × 0.25	0.45 × 0.45 × 0.45	0.12 × 0.17 × 0.09
F(000)	1920	3304	3144
absorption coeff. (mm^{-1})	0.409	0.423	0.780
θ range (deg) for data collection	2.19−23.28	2.29−23.28	0.87−23.31
index ranges	$-21 \le h \le 22$	$-16 \le h \le 17$	$-26 \le h \le 25$
	$-12 \le k \le 8$	$-20 \le k \le 23$	$-27 \le k \le 27$
	$-21 \le l \le 21$	$-27 \le l \le 28$	$-9 \le l \le 14$
reflections collected	17385	31601	19041
independent reflns (R_{int})	6414 (0.0501)	5951 (0.0582)	4642 (0.0705)
completeness to θ_{max}	99.4%	99.8%	99.5%
data/restraints/parameters	6414/0/764	5951/0/482	4642/1/576
GOF[c] on F^2	1.064	1.479	1.111
R1,[a] wR2[b] [$I > 2\sigma(I)$]	0.0345, 0.0840	0.0962, 0.1867	0.0548, 0.1437
R1,[a] wR2[b] (all data)	0.0419, 0.0876	0.0962, 0.1867	0.0571, 0.1463
extinction coefficient	not used	0.00334(18)	not used
largest diff. peak, hole	0.247, −0.315 eÅ^{-3}	1.003, −0.605 eÅ^{-3}	0.827, −0.766 eÅ^{-3}

[a] $R1 = \sum||F_o| - |F_c||/\sum|F_o|$. [b] $wR2 = (\sum(w(F_o^2 - F_c^2)^2)/\sum(w(F_o^2)^2))^{1/2}$. [c] $GOF = (\sum w(F_o^2 - F_c^2)^2/(n - p))^{1/2}$ where n is the number of data and p is the number of parameters refined.

Table 2. Selected Crystallographic Metric Parameters of Iron Porphyrinogens (atom numbering scheme provided in Figure 1)

[(THF)Na(Opy)]$_2$[LFe^{II}]		[Na(diglyme)$_2$][LFe^{III}]		[L$^{\Delta\Delta}$Fe^{II}(NCCH$_3$)][(C$_2$B$_9$H$_{11}$)$_2$Co]$_2$·2CH$_3$CN·2*o*-C$_6$H$_4$Cl$_2$	
			Distances/Å		
Fe(1)−N(1)	1.9185(17)	Fe(1)−N(3)	1.896(5)	Fe(1)−N(1)	2.115(5)
Fe(1)−N(2)	1.9353(17)	Fe(1)−N(4)	1.897(5)	Fe(1)−N(2)	2.117(6)
Fe(1)−N(4)	1.9371(17)	Fe(1)−N(1)	1.899(5)	Fe(1)−N(3)	2.065(8)
Fe(1)−N(3)	1.9430(16)	Fe(1)−N(2)	1.904(5)		
N(1)−C(1)	1.376(3)	N(1)−C(1)	1.375(7)	N(1)−C(4)	1.278(8)
N(1)−C(18)	1.381(3)	N(1)−C(4)	1.393(7)	N(1)−C(1)	1.446(8)
N(2)−C(3)	1.381(3)	N(2)−C(8)	1.379(7)	N(2)−C(8)	1.334(8)
N(2)−C(6)	1.385(3)	N(2)−C(11)	1.387(7)	N(2)−C(11)	1.447(9)
C(1)···C(3)	2.53	C(4)···C(8)	2.47	C(1)−C(1')	1.607(11)
C(6)···C(8)	2.49	C(1)···C(25)	2.48	C(11)−C(11')	1.553(13)
C(11)···C(13)	2.49	C(11)···C(15)	2.48	C(4)···C(8)	2.47
C(16)···C(18)	2.51	C(18)···C(22)	2.46		
			Angles/deg		
N(1)−Fe(1)−N(2)	89.55(7)	N(1)−Fe(1)−N(2)	89.6(2)	N(1)−Fe(1)−N(2)	87.27(18)
N(2)−Fe(1)−N(3)	90.49(7)	N(2)−Fe(1)−N(3)	90.1(2)	N(1)−Fe(1)−N(1A)	79.5(3)
N(3)−Fe(1)−N(4)	90.15(7)	N(3)−Fe(1)−N(4)	90.2(2)	N(2A)−Fe(1)−N(2)	78.7(3)
N(4)−Fe(1)−N(1)	89.82(7)	N(4)−Fe(1)−N(1)	90.2(2)	N(1A)−Fe(1)−N(2)	139.77(19)
				N(3)−Fe(1)−N(1)	110.3(2)
				C(1)−C(15)−C(1')	63.3(6)
				C(11)−C(12)−C(11')	62.3(7)
				C(4)−C(5)−C(8)	110.3(4)

through space ("pseudocontact").[108] In the above expression, μ_0 is the vacuum permeability, k Boltzmann's constant, T the absolute temperature, S the electron spin quantum number, and g_{par} and g_{per} the components of the diagonalized **g** tensor of the paramagnetic center that lie parallel and perpendicular to the molecular axis, respectively. By taking the ratio $(\Delta\nu_{pc})_{ax}/(\Delta\nu_{pc})_{eq}$, one only retains the geometric parameters. Equating the coordinates of the methyl hydrogens in solution to the position of the methyl carbon in the solid state, we find that $(\Delta\nu_{pc})_{ax}/(\Delta\nu_{pc})_{eq} = -3.0$ for $[LFe^{III}]^-$ and -4.2 for $[LFe^{II}]^{2-}$; the observed shift ratio between the axial and methyl resonances in Figure 2 is -2.5 for $[LFe^{III}]^-$ and -4.6 for $[LFe^{II}]^{2-}$. Given the crudeness of the geometric approximation, the agreement is reasonable.

The ^{1}H and ^{2}H NMR spectra of $[L^{\Delta\Delta}Fe^{II}]^{2+}$ show a doubling in the number of resonances (Figure 2, bottom trace). This result

(108) Bertini, I.; Luchinat, C. *Physical Methods for Chemists*; Drago, R. S., Ed.; Saunders College: Ft. Worth, 1977; Vol. 3, pp 500−556.

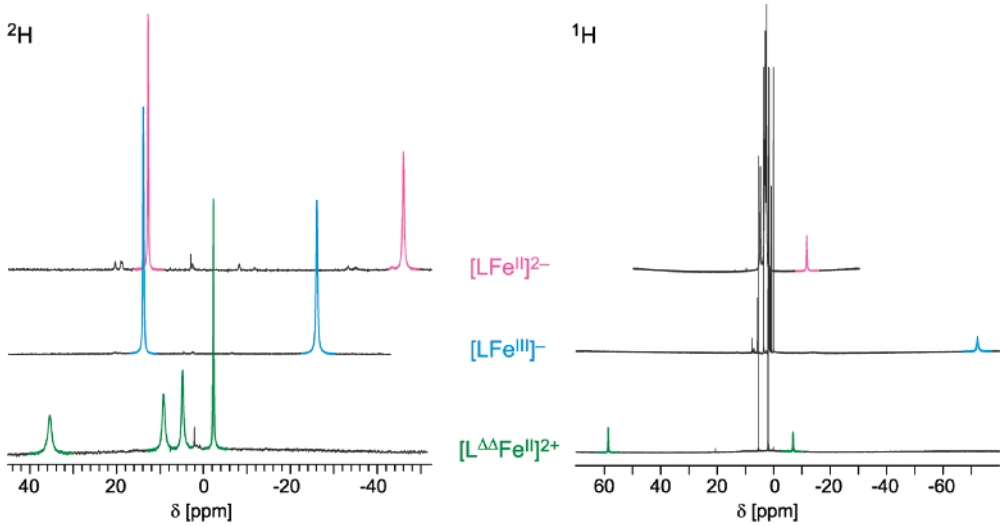

Figure 2. ^{2}H (left) and ^{1}H (right) NMR spectra of the three paramagnetic iron−d_{24}-porphyrinogen species. The ^{2}H NMR (77 MHz, CH_3CN) probes the meso methyl groups, and the ^{1}H NMR (500 MHz, CD_3CN) probes the β pyrrole sites of the porphyrinogen macrocycles.

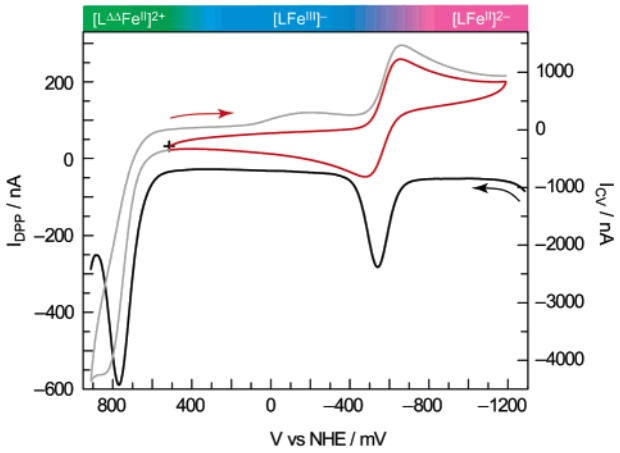

Figure 3. Cyclic voltammetric (red and gray) and differential pulse polarographic (black) traces of a 1 mM CH_3CN solution of $Bu_4N[LFe^{III}]$ and 0.04 M Bu_4NBPh_4. The cyclic voltammogram was recorded at a sweep rate of 100 mV/s and the differential pulse voltammogram at a sweep rate of 20 mV/s, pulse amplitude of 20 mV, pulse period of 200 ms, pulse width of 50 ms, and sample width of 17 ms. The color-coded stripe identifies the predominant iron porphyrinogen species in each potential range.

is in line with the observed lowering in symmetry of the solid-state structure upon oxidation of the macrocycle. Thus, the symmetry properties of the porphyrinogen system are revealed in their quintessential simplicity by appropriate deuteration of the tetrapyrrole.

Electrochemistry. Figure 3 shows the cyclic voltammogram of $[LFe^{III}]^-$ in CH_3CN. Two oxidation−reduction events are observed. Reversible electrochemical behavior for the cyclic voltammetric process at $E_{1/2} = -0.57$ V (vs NHE) is indicated by linear plots of the cathodic and anodic currents vs $v^{1/2}$ (scan rate, v: 50−600 mV s^{-1}) (Figure S2) and values of 1.2 ± 0.2 for the ratios of the anodic and cathodic peak currents. The redox process at more positive potential is characterized by a significant increase in the current response and an irreversible wave form. As is often the case, a potential for the redox process is afforded by differential pulse polarography. An anodically scanning electrode immersed in CH_3CN solutions of $[LFe^{III}]^-$ yields two peaks in the differential pulse polarogram. The process at $E_p = -0.55$ V (vs NHE) corresponds to the reversible $E_{1/2} = -0.57$ V wave observed in the cyclic voltammogram. The process at $E_p = 0.77$ V (vs NHE) corresponds to a multielectron reaction; its peak current is ~3 times greater than that of the reversible process. A more accurate measurement of the redox equivalency for both electrode processes is afforded by chronocoulometry. Using the Cottrell equation, plots of Q vs $t^{1/2}$ for potential steps encompassing the $E_p = -0.55$ and $E_p = 0.77$ redox processes yield a linear response with slopes in 1:2.7 ratio, consistent with the DPP result. The identities of these two electrode processes are revealed by performing electrochemical experiments on solutions of $[L^{\Delta\Delta}Fe^{II}]^{2+}$: differential pulse polarograms exhibit identical peaks with those displayed in Figure 3. Taken together, the DPP, CV, and chronocoulometric results lead us to the following electrochemical assignments:

$$[LFe^{III}]^- + e^- \rightarrow [LFe^{II}]^{2-} \quad E_{1/2} = -0.57 \text{ V} \qquad (3)$$

$$[L^{\Delta\Delta}Fe^{II}]^{2+} + 3e^- \rightarrow [LFe^{III}]^- \quad E_p = +0.77 \text{ V} \qquad (4)$$

We note that peak potential measurements for quasi-reversible and irreversible processes in DPP will be shifted to more negative potentials by an activation overpotential. Notwithstanding, fast cyclic voltammetric scans of the $[L^{\Delta\Delta}Fe^{II}]^{2+}/[LFe^{III}]^-$ couple indicate that E_p is near $E_{1/2}$.

The porphyrinogen macrocycle is very electron-donating as reflected by the reduction potential of the iron residing at its core. The reduction potential of reaction 3 is more negative than that of low-potential ferrodoxins (Fd), whose ferric forms are among the most difficult iron cofactors to reduce in biology ($E_{1/2}(FdFe^{III/II}) = 0$ to -0.5 V vs NHE).[109] With regard to its porphyrin relatives, iron porphyrinogen is ~0.5 to 1.3 V more difficult to reduce than heme cofactors (depending on the nature of the axial ligands).

Reaction 4 provides a measure of ligand-centered redox processes. The porphyrinogen can react in two-electron steps with the concomitant formation of a C−C bond between the α carbons of adjacent pyrroles; each cyclopropane thus formed is a two-equivalent hole reservoir for the porphyrinogen framework. The reduction potentials of half-reactions 3 and 4

(109) Battistuzzi, G.; D'Onofrio, M.; Borsari, M.; Sola, M.; Macedo, A. L.; Moura, J. J. G.; Rodrigues, P. *J. Biol. Inorg. Chem.* **2000**, *5*, 748−760.

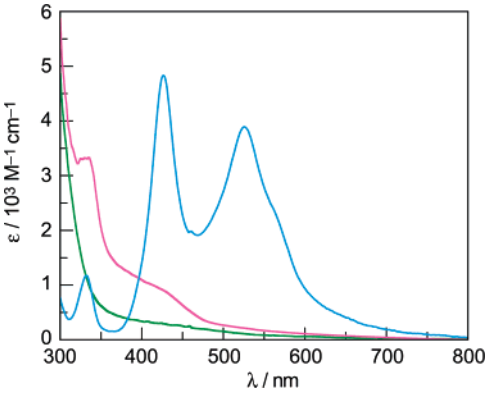

Figure 4. UV−visible absorption spectra of $Na_2(THF)_2[LFe^{II}]$ (pink spectrum), $Na(THF)_2[LFe^{III}]$ (blue spectrum), and $[L^{\Delta\Delta}Fe^{II}](BF_4)_2$ (green spectrum) in CH_3CN.

offer the potential for the overall four-electron ligand-based reduction

$$[L^{\Delta\Delta}Fe^{II}]^{2+} + 4e^- \rightarrow [LFe^{II}]^{2-} \quad E_{1/2} = 0.43\ V \qquad (5)$$

The four-electron reduction of the porphyrinogen macrocycle was previously ascertained by inserting the redox-inactive Zn^{2+} ion into the porphyrinogen macrocycle.[90] For this system the consecutive two-electron processes were observed at $E_{1/2}([L^{\Delta\Delta}Zn^{II}]^{2+}/[L^{\Delta}Zn^{II}]) = 0.63$ V and $E_{1/2}([L^{\Delta}Zn^{II}]/[LZn^{II}]^{2-}) = 0.21$ V vs NHE. Combining these two redox couples yields a potential for the overall four-electron ligand-centered reduction

$$[L^{\Delta\Delta}Zn^{II}]^{2+} + 4e^- \rightarrow [LZn^{II}]^{2-} \quad E_{1/2} = 0.42\ V \qquad (6)$$

The consistency between the ligand redox potentials for half-reactions 5 and 6 for macrocycles encrypting redox-active and redox-inactive metals suggests that the frontier orbitals of the ligand are not significantly perturbed by the metal orbitals residing at its core.

The inability to observe the partially oxidized porphyrinogen species for iron, when it is available to zinc, suggests that the disproportionation of $[L^{\Delta}Fe^{II}]$ to the observed iron porphyrinogens is favorable

$$3[L^{\Delta}Fe^{II}] \rightarrow 2[LFe^{III}]^- + [L^{\Delta\Delta}Fe^{II}]^{2+} \qquad (7)$$

We can assess the viability of this contention if we assume that the potentials for the two-electron ligand transformations are the same for iron and zinc, i.e., $E_{1/2}([L^{\Delta\Delta}M^{II}]^{2+}/[L^{\Delta}M^{II}]) = 0.63$ V and $E_{1/2}([L^{\Delta}M^{II}]/[LM^{II}]^{2-}) = 0.21$ V vs NHE for M = Zn and Fe. This assumption is reasonable, given that we have already shown the reduction potentials for half-reactions 5 and 6 to be nearly equivalent. On this basis, we calculate the following reduction potential:

$$[L^{\Delta}Fe^{II}] + e^- \rightarrow [LFe^{III}]^- \quad E_{1/2} = 0.99\ V \qquad (8)$$

With this in hand, the driving force for reaction 7 is determined to be $\Delta E(7) = +0.36$ V. In contrast to the zinc porphyrinogen case, the availability of the +3 metal oxidation state and the stability of the $[LM^{III}]^-$ species drives disproportionation reaction 7, thus preventing the isolation of $[L^{\Delta}Fe^{II}]$.

Electronic Structure of Iron Porphyrinogens. Solutions of $[LFe^{III}]^-$ are blood red, whereas those of $[LFe^{II}]^{2-}$ are pale yellow and those of $[L^{\Delta\Delta}Fe^{II}]^{2+}$ even paler in color. Figure 4 reproduces the absorption spectra of $[LFe^{II}]^{2-}$, $[LFe^{III}]^-$, and $[L^{\Delta\Delta}Fe^{II}]^{2+}$ in CH_3CN. The intense color of $[LFe^{III}]^-$ arises from two bands at 427 and 526 nm that dominate the absorption profile; a ~570 nm shoulder is observed on the trailing edge of the lowest-energy absorption band. The molar absorption coefficients of both bands suggest a charge-transfer parentage for the transitions. A ligand-to-metal character for this charge-transfer concurs with the very reducing nature of the $[L]^{4-}$ ligand and the presence of an oxidizing Fe^{III} center. The featureless profiles of both $[LFe^{II}]^{2-}$ and $[L^{\Delta\Delta}Fe^{II}]^{2+}$ support this LMCT assignment: reduction of the metal and oxidation of the ligand would cause a LMCT to blue shift into the ultraviolet spectral region. Accordingly, a charge-transfer absorption is not observed for either compound.

More quantitative insight into the frontier molecular orbitals of the iron porphyrinogens is provided by DFT calculations. Full geometry optimizations on $[Na(THF)_2]_2[LFe^{II}]$ and $[Na(THF)_2][LFe^{III}]$ were performed, and the Na^+ ions and their attendant coordination spheres were removed to afford the isolated porphyrinogen frameworks. The optimized geometry and the details of the MO diagram for these calculations were found to reproduce those obtained for single-point calculations of $[LFe^{II}]^{2-}$ and $[LFe^{III}]^-$ at the geometries imposed by the crystal structures of $[(THF)Na(Opy)]_2[LFe^{II}]$ and $[Na(digly)_2][LFe^{III}]$. On the basis of these results, the electronic structure of $[L^{\Delta\Delta}Fe^{II}(NCCH_3)]^{2+}$ was determined from a single-point calculation at the geometry defined by the crystal structure of $[L^{\Delta\Delta}Fe^{II}(NCCH_3)][(C_2B_9H_{11})_2Co]_2$. This approach allowed us to circumvent the significant computational effort and complexity associated with treating the $[(C_2B_9H_{11})_2Co]^-$ anions. Orbital energies and Mulliken populations for the iron porphyrinogens are listed in the Supporting Information (Tables S26−S31).

Figure 5 displays the energy level diagrams and the Kohn−Sham representations of the frontier molecular orbitals of $[LFe^{II}]^{2-}$ and $[LFe^{III}]^-$. Because spin restriction is lifted, there is no common spatial wave function for each α/β spin pair, and accordingly, two manifolds of "orbitals" are represented for the α and β spinors. Pairs of spinors with antiparallel spin and similar spatial extension for the metal-based functions are correlated by dashed lines. We note that the Kohn−Sham orbitals differ from those derived from a Hartree−Fock (HF) formalism by the inclusion of the exchange correlation energy;[110] however, comparative analysis establishes that the shapes and symmetries of the Kohn−Sham orbitals accord well with those calculated by more traditional HF and extended Hückel approximations,[111,112] and indeed these orbitals have found widespread use in electronic structure descriptions.[113−120] The

(110) Kohn, W.; Becke, A. D.; Parr, R. G. *J. Phys. Chem.* **1996**, *100*, 12974−12980.
(111) Stowasser, R.; Hoffmann, R. *J. Am. Chem. Soc.* **1999**, *121*, 3414−3420.
(112) Hamel, S.; Duffy, P.; Casida, M. E.; Salahub, D. R. *J. Electron Spectrosc. Relat. Phenom.* **2002**, *123*, 345−363.
(113) Lehnert, N.; Neese, F.; Ho, R. Y. N.; Que, L., Jr.; Solomon, E. I. *J. Am. Chem. Soc.* **2002**, *124*, 10810−10822.
(114) Chen, P.; Root, D. E.; Campochiaro, C.; Fujisawa, K.; Solomon, E. I. *J. Am. Chem. Soc.* **2003**, *125*, 466−474.
(115) Chisholm, M. H.; Gallucci, J.; Hadad, C. M.; Huffman, J. C.; Wilson, P. J. *J. Am. Chem. Soc.* **2003**, *125*, 16040−16049.
(116) Gray, T. G.; Rudzinski, C. M.; Meyer, E.; Holm, R. H.; Nocera, D. G. *J. Am. Chem. Soc.* **2003**, *125*, 4755−4770.
(117) Gray, T. G.; Rudzinski, C. M.; Meyer, E. E.; Nocera, D. G. *J. Phys. Chem. A* **2004**, *108*, 3238−3243.
(118) Chang, C. J.; Loh, Z.-H.; Shi, C.; Anson, F. C.; Nocera, D. G. *J. Am. Chem. Soc.* **2004**, *126*, 10013−10020.
(119) Manke, D. R.; Loh, Z.-H.; Nocera, D. G. *Inorg. Chem.* **2004**, *43*, 3618−3624.

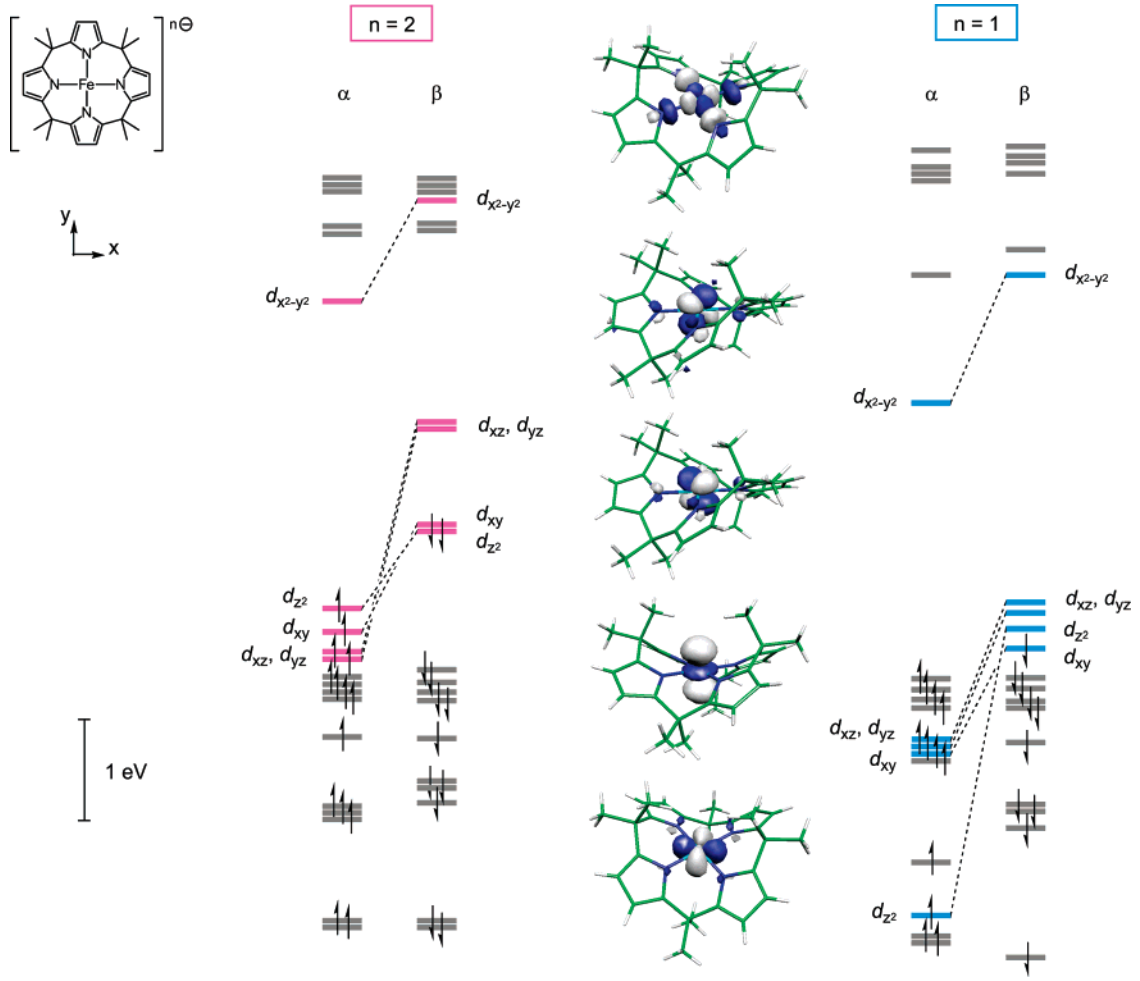

Figure 5. Molecular orbital diagram for $[LFe^{II}]^{2-}$ (left) and $[LFe^{III}]^{-}$ (right), with metal-centered functions highlighted in color. Because spin restriction is lifted, there is not a common spatial wave function for each α/β spin pair, and two manifolds of "orbitals" are drawn separately. The metal-centered spatial wave functions are similar for $[LFe^{II}]^{2-}$ and $[LFe^{III}]^{-}$ and for α and β spinors. The orbitals shown in the middle of the diagram are depicted at the 95% probability level for the β spinors of $[LFe^{III}]^{-}$.

relative energies and characters of the molecular orbitals for the iron porphyrinogen in both Fe^{III} and Fe^{II} oxidations states are similar. As expected, the d-orbitals of the more electropositive Fe^{III} center are slightly stabilized with respect to those of its Fe^{II} congener. Both $[LFe^{II}]^{2-}$ and $[LFe^{III}]^{-}$ are predicted to assume intermediate spin arising from the electronic configurations $(d_{xy})^2(d_{z^2})^2(d_{xz},d_{yz})^2(d_{x^2-y^2})^0$ and $(d_{xy})^2(d_{z^2})^1(d_{xz},d_{yz})^2(d_{x^2-y^2})^0$, respectively (Table S32). The d_{xy}, d_{xz}, and d_{yz} orbitals are effectively nonbonding as is the d_{z^2} orbital in the absence of an axial ligand. Conversely, the $d_{x^2-y^2}$ is strongly destabilized by its σ-antibonding interaction with the pyrrole lone pairs, thus accounting for the inaccessibility of the high spin state. We find that >99% of the overall unpaired spin is carried within the d orbital manifold, with little spin observed about the porphyrinogen periphery. This result is highlighted by the Kohn−Sham representations for the frontier molecular orbitals, which are similar for the α and β spinors of both $[LFe^{II}]^{2-}$ and $[LFe^{III}]^{-}$. For brevity, the spatial representations for the spinors of $[LFe^{III}]^{-}$ are depicted in the center of Figure 5. These frontier orbitals exhibit nearly exclusive metal d orbital character with no contribution from the porphyrinogen framework. This result is consistent with electrochemical measurements, which reveal that the ligand-based oxidation is not affected by the nature of the metal ion as evidenced by the similarity of the redox potentials for half-reactions 5 and 6.

The ligand field of the oxidized porphyrinogen, $L^{\Delta\Delta}$, is significantly weakened relative to that of $[L]^{4-}$, to the extent that Fe^{II} in $[L^{\Delta\Delta}Fe^{II}(NCCH_3)]^{2+}$ assumes a high-spin electron configuration. Figure 6 displays the Kohn−Sham orbitals of $[L^{\Delta\Delta}Fe^{II}(NCCH_3)]^{2+}$. The ~4 eV span for the d-orbital splitting in $[LFe]^{n-}$ complexes is reduced to ~1.5−2 eV in $[L^{\Delta\Delta}Fe^{II}(NCCH_3)]^{2+}$. The diminished ligand field arises from the confluence of a smaller metal−ligand σ interaction and a decreased basicity of the oxidized ligand. The former effect results from the distortion of the $L^{\Delta\Delta}$ porphyrinogen macrocycle from the perfect square coordination geometry that characterizes the $[L]^{4-}$ ligand environment. The most significant perturbation of this distortion is the stabilization of the $d_{x^2-y^2}$ orbital, thus allowing for its occupation by an unpaired electron, and this yields a high-spin state ($S = 2$). The decreased basicity is a direct consequence of the oxidation of the macrocycle by four electrons. As for the complexes of the fully reduced ligand, more than 99% of the total unpaired spin is localized on the iron center.

The nature of the symmetry lowering of the macrocycle upon four-electron oxidation is abundantly clear from the comparison

(120) Gray, T. G.; Veige, A. S.; Nocera, D. G. *J. Am. Chem. Soc.* **2004**, *12*, 9760−9768.

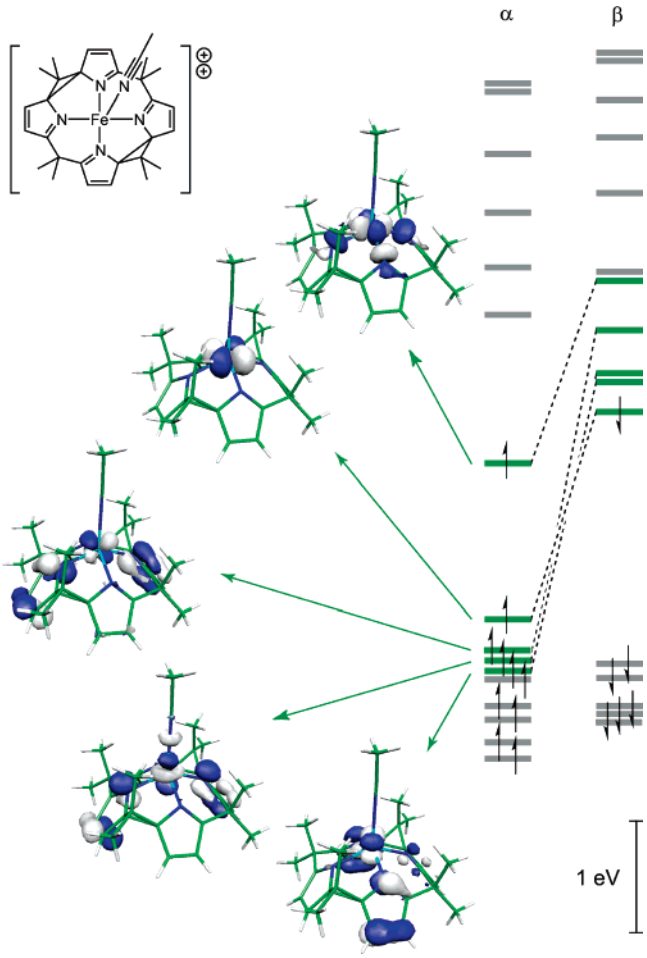

Figure 6. Molecular orbital diagram for $[L^{\Delta\Delta}Fe^{II}(NCCH_3)]^{2+}$ with metal-centered functions highlighted in color. Because spin restriction is lifted, there is not a common spatial wave function for each α/β spin pair, and two manifolds of "orbitals" are drawn separately. The metal-centered spatial wave functions are depicted at the 95% probability level for the α spinors of $[L^{\Delta\Delta}Fe^{II}(NCCH_3)]^{2+}$.

of the frontier molecular orbitals of $[L]^{4-}$ and $L^{\Delta\Delta}$ shown in Figure 7. The $[L]^{4-}$ macrocycle in $[LFe^{II}]^{2-}$ and $[LFe^{III}]^{-}$ features four, essentially degenerate, HOMOs that arise from the four possible combinations of the a_2 π orbitals of the constituent pyrroles to yield one completely bonding combination (with respect to the interpyrrole $C^{\alpha}\cdots C^{\alpha}$ interactions), a completely antibonding one, and each of the last two featuring two bonding and two antibonding nearest-neighbor $C^{\alpha}\cdots C^{\alpha}$ interactions. In the ruffled conformation of $[L]^{4-}$, the four pyrroles are electronically isolated from each other, and the four linear combinations are isoenergetic and completely occupied (eight electrons) to give a net bond order of zero. As schematically represented in Chart 2, four-electron oxidation of this set of frontier molecular orbitals lifts the four-fold degeneracy (left panel). The four remaining electrons pair up in the two orbitals that are bonding with respect to the newly established $C^{\alpha}-C^{\alpha}$ bonds, yielding a net bond order of two. If only the nodal structure between pyrroles is represented (bottom left panel), then the overall stereoelectronic transformation between $[L]^{4-}$ and $L^{\Delta\Delta}$ becomes reminiscent of the classic problem in physical organic chemistry—the distortion of the square cyclobutadiene dianion (with four electrons in two, filled, degenerate π orbitals) to the rectangular cyclobutadiene upon removal of half of its highest-lying π electrons (bottom right panel). The tetrapyrrole

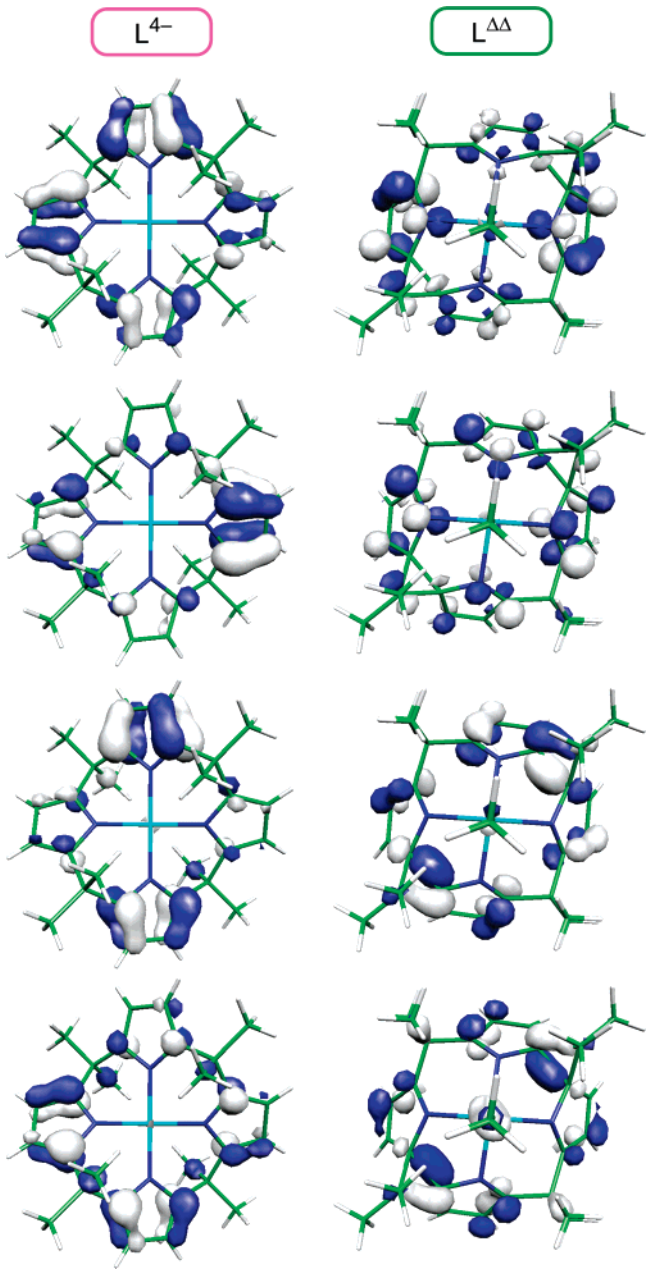

Figure 7. Comparison of relevant ligand-based Kohn−Sham orbitals of π-type symmetry for $[L]^{4-}$ and $L^{\Delta\Delta}$.

oxidation is a four-electron equivalent of that of the cyclobutadiene dianion; in both cases, the oxidized species has to distort from the four-fold symmetric geometry to lift the frontier orbital degeneracy, yielding two diametrically situated bonds.

Electronic Structure Measurements. The electronic structure calculations predict $S = 1$, $^3/_2$, and 2 ground states for $[LFe^{II}]^{2-}$, $[LFe^{III}]^{-}$, and $[L^{\Delta\Delta}Fe^{II}]^{2+}$, respectively (Figures 5 and 6, Table S32). Experimentally, the half-integer spin of $[LFe^{III}]^{-}$ could be assessed easily by EPR: the spectrum of $(Bu_4N)[LFe^{III}]$ is shown in the top of Figure 8. It is similar those of Fe^{III} ($S = {}^3/_2$) ions residing in the square ligand fields of corroles and porphyrins in the absence of axial ligands.[121,122] The observed g values of 4.2 (at $\partial A/\partial H = 0$) and 1.95 (at $\partial^2 A/\partial H^2 = 0$) are

(121) Sakai, T.; Ohgo, Y.; Ikeue, T.; Takahashi, M.; Takeda, M.; Nakamura, M. *J. Am. Chem. Soc.* **2003**, *125*, 13028−13029.
(122) Simkhovich, L.; Goldberg, I.; Gross, Z. *Inorg. Chem.* **2002**, *41*, 5433−5439.

Chart 2

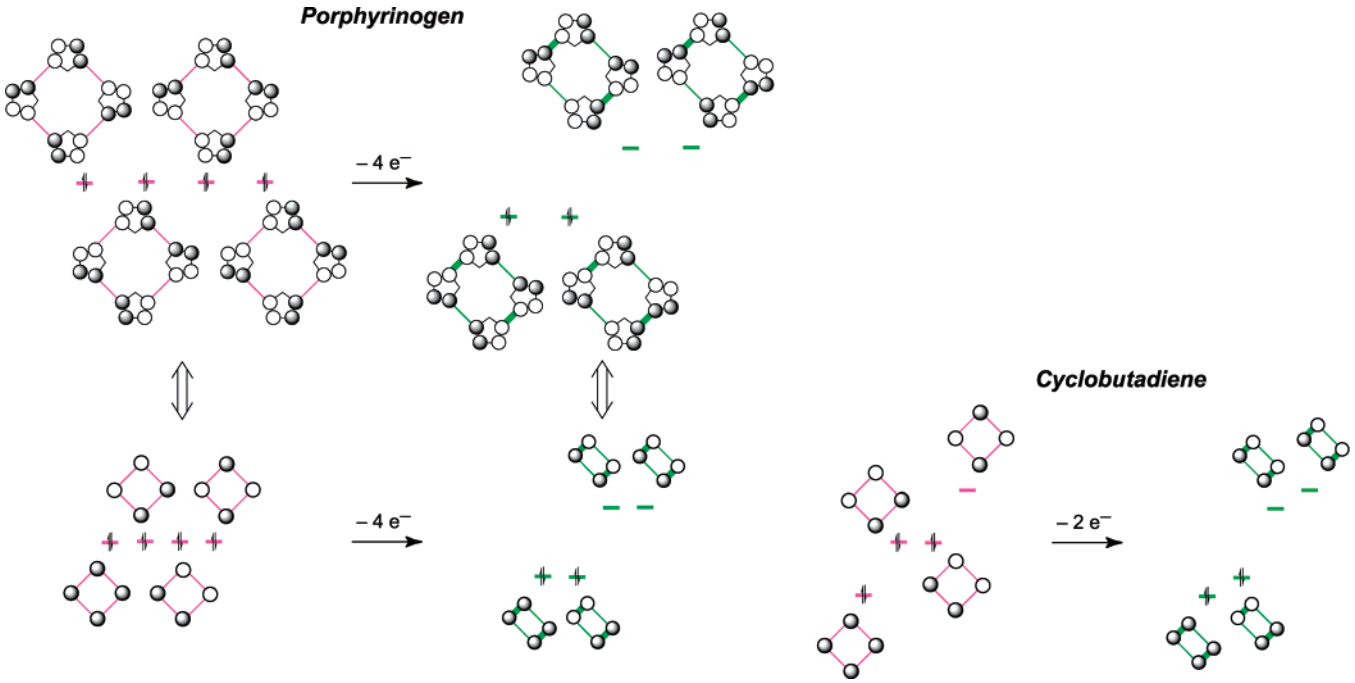

typical of an intermediate-spin Fe^{III} ($g_x = g_y = 4$, $g_z = 2$) with large axial zero-field splitting (zfs) ($D \gg h\nu$) but no rhombic asymmetry ($E/D = 0$).[123] These zfs features are in agreement with the D_{2d} symmetry of the tetrapyrrole complexes. Per the results of Sakai et al.,[121] the small high-field deviation from $g_z = 2$ indicates a single-electron occupancy for d_{xz}, d_{yz} and d_{z^2}; this result is also obtained theoretically, as shown in Figure 5. Spectra of more dilute samples exhibit a very complicated fine structure which we did not try to interpret. Consistent with these EPR results, the magnetism of $[LFe^{III}]^-$ complies with the Curie−Weiss law, including temperature-independent paramagnetism (TIP), yielding an effective moment of $\mu_{eff} = 3.7$ β, which is near the spin-only value for $S = {}^3/_2$ ($\mu_{eff} = 3.87$, $g = 2$).

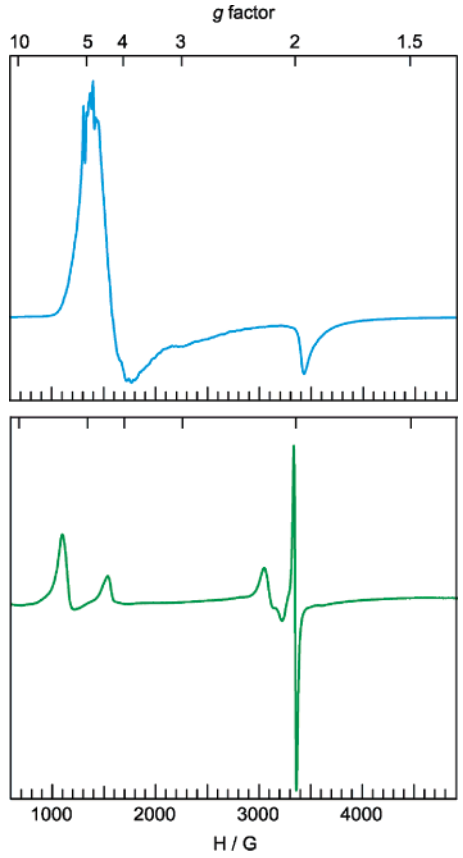

Figure 8. Frozen solution X-band (9.385 GHz) EPR spectra of $(Bu_4N)[LFe^{III}]$ (blue spectrum) in frozen THF (4.5 K) and $[L^{\Delta\Delta}Fe^{II}](BF_4)_2$ (green spectrum) in frozen CH_3CN (4.5 K). $[LFe^{II}]^{2-}$ is EPR silent.

As integer-spin systems, $[LFe^{II}]^{2-}$ and $[L^{\Delta\Delta}Fe^{II}]^{2+}$ are less amenable to EPR investigation. Indeed, $(Bu_4N)_2[LFe^{II}]$ was found to be EPR silent, consistent with the presence of a large zero-field splitting (zfs) ($D \gg h\nu$, $E/D = 0$). The observation of an EPR spectrum (Figure 8, bottom) for $[L^{\Delta\Delta}Fe^{II}](BF_4)_2$ indicates rhombic distortion from a square coordination, $E/D \neq 0$. The formation of both cyclopropane rings, observed by crystallography and by NMR, presumably results in $|m_s|$ state mixing, giving rise to otherwise forbidden transitions. A Curie−Weiss fit of the magnetism of $[L^{\Delta\Delta}Fe^{II}](BF_4)_2$ yields an overall $\mu_{eff} = 5.0$ β (μ_{eff}(calcd) $= 4.9$ β for spin-only $S = 2$).

Definitive experimental oxidation state and spin state assignments for the inorganic centers of $[LFe^{II}]^{2-}$ and $[L^{\Delta\Delta}Fe^{II}]^{2+}$ were afforded by their Mössbauer spectra, displayed in Figure 9. The single quadrupole doublet exhibited by $[LFe^{II}]^{2-}$ ($\delta = 0.35$ mm/s, $\Delta E_q = 2.34$ mm/s) is characteristic of an intermediate spin, $S = 1$. Although this spin state is relatively rare for Fe^{II}, it is by far the most prevalent in the few reported square planar complexes of that ion, and the Mössbauer characteristics lie within the range spanned by these complexes.[124−126] The

(123) Palmer, G. In *Physical Methods in Bioinorganic Chemistry*; Que, L., Jr., Ed.; University Science Books: Sausalito, CA, 2000; p 153.
(124) Oh, Y.; Shin, B.-C.; Swenson, D.; Goff, H. M.; Kang, S. K. *Acta Crystallogr.* **2004**, *C60*, m57−m59.
(125) Strauss, S. H.; Silver, M. E.; Long, K. M.; Thompson, R. G.; Hudgens, R. A.; Spartalian, K.; Ibers, J. A. *J. Am. Chem. Soc.* **1985**, *107*, 4207−4215.
(126) Riley, D. P.; Stone, J. A.; Busch, D. H. *J. Am. Chem. Soc.* **1977**, *99*, 767−767.

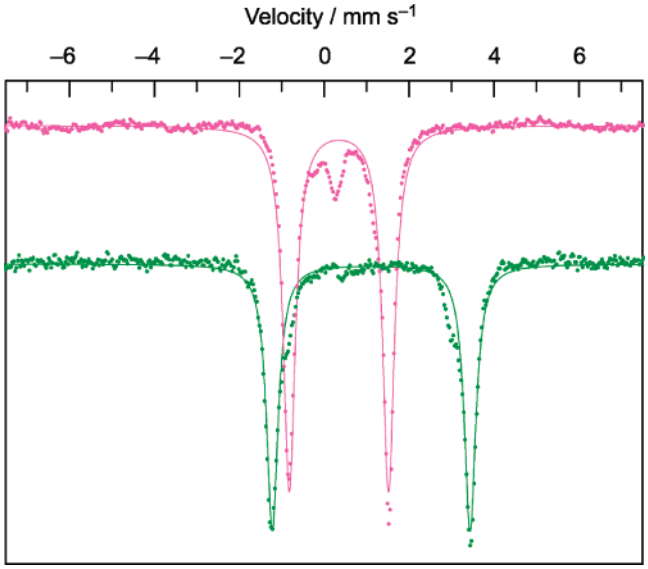

Figure 9. ^{57}Fe Mössbauer spectra of powdered $Na_2(THF)_2[LFe^{II}]$ (top) and $[L^{\Delta\Delta}Fe^{II}](BF_4)_2$ (bottom) at 4.2 K.

Mössbauer spectrum of the $[L^{\Delta\Delta}Fe^{II}]^{2+}$ cation ($\delta = 1.11$ mm/s, $\Delta E_q = 4.66$ mm/s) is most intriguing. The large quadrupole splitting clearly indicates a high spin state, $S = 2$;[127] but also, this ΔE_q is to the best of our knowledge the largest reported to date, surpassing the value of 4.55 mm/s that is observed for the distorted tetrahedral Fe^{II} ($S = 2$) center in $[Fe_3(SC_6H_2{}^iPr_3\text{-}2,4,6)_4\{N(SiMe_3)_2\}_2]$.[128]

Conclusions

Three oxidation states of iron porphyrinogen have been unveiled in the absence of any redox or spectroscopically active counterions. A metal-centered $Fe^{II/III}$ redox activity, reminiscent of heme porphyrins, is observed. Owing to the highly reducing nature of the tetrapyrrole framework, the $Fe^{III/II}$ reduction potential, however, is nearly one volt more negative than that of a typical heme cofactor. This metal-based redox activity is augmented by a multielectron chemistry of the porphyrinogen macrocycle. Two cyclopropane rings, formed from the C−C coupling between the α carbons of adjacent pyrroles, function as two separate two-hole reservoirs within the porphyrinogen framework. The two-electron oxidized, singly C^α−C^α bonded, intermediate is unstable with respect to disproportionation; the ligand-based redox activity therefore proceeds in a single four-electron step. The oxidation of the tetrapyrrole is accompanied by a distortion of the 4-N core from a square to a rectangle, and this structural deformation is manifest to the electronic structure of the different iron porphyrinogens.

The ability of the tetrapyrrole macrocycle to support redox transformations in addition to the metal establishes "artificial hemes" as more versatile redox cofactors than hemes. This redox activity between the metal and the ligand is decoupled from the acid−base activity of the iron center. Large variations in the overall redox content can be accommodated without any changes in the metal's primary coordination sphere. This is drastically different from the usual observation of a metal center that will have its coordination geometry and/or number change upon multielectron oxidation. For the case of iron hemes, oxidation is typically accompanied by an increase in metal−substrate bond order (e.g., oxo). It can be anticipated that iron porphyrinogens bearing halogen- or chalcogen-based ligand substrates will maintain more labile metal−substrate bonds in high oxidation states. We are currently pursuing such ideas in the context of the activation of small molecules.

Acknowledgment. We dedicate this work to the memory of Prof. Carlo Floriani, a pioneer in the chemistry of porphyrinogens. We thank B. M. Bartlett for acquiring the SQUID data, Prof. S. J. Lippard for use of his Mössbauer instrument, and Dr. J. Kuzelka and Dr. S. Yoon for their help with its use. This work was supported by a grant from the National Science Foundation (CHE-0132680). J.B. gratefully acknowledges MIT for a pre-doctoral Presidential Fellowship and the Shell Oil Company for a research fellowship.

Supporting Information Available: Crystal structure of $[(THF)_3Fe^{II}(\mu\text{-}Cl)_3Fe^{II}(THF)_3][(THF)_4Fe^{II}(\mu\text{-}Cl)_2Fe^{II}(THF)_4]_{1/2}[LFe^{III}]_2\cdot 2PhCH_3$; cyclic voltammetry of the $[LFe^{III}]^-/[LFe^{II}]^{2-}$ redox couple; atom numbering schemes, tables of crystal data, atomic coordinates, bond lengths and angles, anisotropic thermal parameters and hydrogen coordinates for $[Na(digly)_2][LFe^{III}]$, $[(THF)_3Fe^{II}(\mu\text{-}Cl)_3Fe^{II}(THF)_3][(THF)_4Fe^{II}(\mu\text{-}Cl)_2Fe^{II}(THF)_4]_{1/2}[LFe^{III}]_2\cdot 2PhCH_3$, $[(THF)Na(Opy)]_2[LFe^{II}]$, and $[L^{\Delta\Delta}Fe^{II}(NCMe)][(C_2B_9H_{11})_2Co]_2\cdot 2MeCN\cdot 2o\text{-}C_6H_4Cl_2$; energies of the frontier MOs and Mulliken population analysis for $[LFe^{II}]^{2-}$, $[LFe^{III}]^-$, and $[L^{\Delta\Delta}Fe^{II}(NCMe)]^{2+}$. X-ray crystallographic files, in CIF format. This material is available free of charge via the Internet at http://pubs.acs.org.

JA043132R

(127) Münck, E. In *Physical Methods in Bioinorganic Chemistry*; Que, L., Jr., Ed.; University Science Books: Sausalito, CA, 2000; p 291.
(128) Evans, D. J. *Chem. Phys. Lett.* **1996**, *255*, 134−136.